NACA

RESEARCH MEMORANDUM

EFFECT OF A HOT-JET EXHAUST ON PRESSURE DISTRIBUTIONS

AND EXTERNAL DRAG OF SEVERAL AFTERBODIES ON A

SINGLE-ENGINE AIRPLANE MODEL AT

TRANSONIC SPEEDS

By Harry T. Norton, Jr., and John M. Swihart

Langley Aeronautical Laboratory
Langley Field, Va.

NATIONAL ADVISORY COMMITTEE
FOR AERONAUTICS
WASHINGTON

NATIONAL ADVISORY COMMITTEE FOR AERONAUTICS

RESEARCH MEMORANDUM

EFFECT OF A HOT-JET EXHAUST ON PRESSURE DISTRIBUTIONS

AND EXTERNAL DRAG OF SEVERAL AFTERBODIES ON A

SINGLE-ENGINE AIRPLANE MODEL AT

TRANSONIC SPEEDS

By Harry T. Norton, Jr., and John M. Swihart

SUMMARY

An investigation of the jet effects on several afterbody shapes of
a single-engine fighter-airplane model has been conducted in the Langley
16-foot transonic tunnel at Mach numbers from 0.80 to 1.10 and angles of
attack from 0° to 5°. The afterbody-geometry variables were boattail
angle, afterbody length, and base area. The primary jet total-pressure
ratio was varied from 1 (jet off) to 7 for primary jet diameters corre-
sponding to afterburning and nonafterburning nozzles. A hydrogen peroxide
gas generator with a scaled convergent nozzle and ejector simulated the
turbojet-engine-ejector installation. This paper presents pressure
distributions and afterbody and base pressure-drag results from the
investigation.

In general, the afterbody drag coefficients varied in the same
manner as the drag of isolated afterbodies; namely, the drag was reduced
by increasing afterbody length, increasing jet diameter, and decreasing
boattail angle, despite the resulting increase in base-annulus area.
The pressure distributions on the afterbodies and bases varied widely
from that of symmetrical bodies because of assymetry of fuselage and
the presence of tail surfaces. Tail-interference effects were large
and beneficial for an afterbody with large boattail angles and were
detrimental for an afterbody with low boattail angles. For typical
turbojet-engine pressure ratios, the overall performance of the after-
body with the lowest boattail angles was better than that of all other
afterbodies investigated, even though the afterbody experienced large
detrimental jet effects.

INTRODUCTION

A number of recent investigations of jet effects on simple isolated bodies (e.g., refs. 1 to 4) have shown that the afterbody fairing around the jet exit may contribute a substantial increment to the overall drag of the airplane. This research has outlined the geometric variables for obtaining the general design requirements of low drag and high effective engine thrust. A broad understanding has not been obtained as yet, however, with regard to interference effects introduced by other components of the airplane and how best to minimize thrust and drag penalties associated with variable engine-exit geometry. This latter problem is of particular importance in the case of the present dash-type supersonic-speed airplane which, in order to attain useful range, must cruise at high subsonic speeds with the afterburner shut off and, consequently, has larger boattail angle, greater base area, or more nozzle expansion than in afterburner-on flight.

As a first step in the study of the aforementioned problems of practical airplanes, an investigation of the afterbody-drag and engine-thrust characteristics of a single-engine fighter-airplane model has been conducted in the Langley 16-foot transonic tunnel. The model was supported from its wing tips and was provided with a number of alternate afterbody shapes varying in length, boattail angle, and base area. A hydrogen peroxide gas generator (ref. 5) was used to provide hot-exhaust jets simulating both the nonafterburner and afterburner-on operating conditions. Measurements of body-tail forces, engine thrust, and afterbody and base pressures were obtained at Mach numbers from 0.80 to 1.10 at angles of attack from $0°$ to $5°$. At each Mach number, the primary jet total-pressure ratio was varied from 1 (jet off) to 7 and for some conditions to 9. The present paper presents the pressure-distribution data obtained on the rear portions of the afterbody and analyzes these data with regard to loads, drag, and flow interference.

SYMBOLS AND ABBREVIATIONS

A   cross-sectional area, sq in.

A/B   afterburner

AR   aspect ratio

C_D drag coefficient, $\sum \dfrac{C_p A_l}{S}$

C_p pressure coefficient, $\dfrac{p_l - p_\infty}{q_\infty}$

c local chord

c' mean aerodynamic chord

d diameter

H_2O_2 hydrogen peroxide

i_t incidence angle of horizontal tail, relative to fuselage center line, deg

l length from base, positive rearward, in.

M Mach number

p static pressure, lb/sq ft

p_t total pressure, lb/sq ft

$p_{t,j}/p_\infty$ ratio of primary jet total pressure to free-stream static pressure

q_∞ free-stream dynamic pressure, lb/sq ft

S wing surface area, sq ft

T stagnation temperature, $^\circ R$ unless otherwise specified

W weight flow, lb/sec

$\dfrac{W_s}{W_p}\sqrt{\dfrac{T_s}{T_p}}$ secondary-to-primary weight-flow ratio

Z equivalent body diameter based on area at 55-inch-fuselage station

Λ sweepback angle, deg

β boattail angle, measured in plane normal to plane of base, deg

ϕ meridian angle, positive clockwise from top center line, deg

Subscripts:

a   afterbody

b   base

ht   horizontal tail

j   jet

l local

m   model

p   primary

r   root

s   secondary, ejector spacing

t   tip

∞ free stream

w   wing

APPARATUS AND METHODS

Tunnel and Support System

The investigation was conducted in the Langley 16-foot transonic tunnel, the air flow and power characteristics of which are described in reference 6. The model was supported at its wing tips by the bifurcate sting-support system as shown in figure 1 with the wing forming an integral part of the support system. The fuselage-tail assembly was mounted on a six-component strain-gage balance which was supported by the wing structure.

Model

The model which was so designed that the afterbodies could be interchanged was of a single-engine fighter airplane. Figure 2 is a sketch which gives the general dimensions of the model and support system. Figure 3 shows the geometric characteristics and dimensions of the afterbodies, and table I gives the location of the pressure

orifices. The angle β of each boattail is shown for various meridians, and the average angle decreases from a maximum of 55° on afterbody A to a minimum of about 6° on afterbody D. The decrease in boattail angle is achieved on B and D by increasing the base area and on C by increasing the afterbody length. The base diameter d_b is the equivalent diameter based on the base area (fig. 3(a)).

Figure 4 shows the cross-sectional area progression of the model including the support system. The area progression of the model was slightly altered from that of the airplane by fairing over the engine inlets and adding the bifurcate support system.

Turbojet Simulator

A hydrogen peroxide gas generator with a convergent nozzle and ejector was mounted in the model as shown in figure 2. Reference 5 shows that the hydrogen peroxide gas generator provides a hot jet having almost exactly the same jet boundaries and flow parameters as those of current turbojet engines operating with afterburner off. For the afterburner-on case, the initial jet shapes are almost exactly the same; however, the jet temperature is 1,400° F to 1,600° F lower with hydrogen peroxide than that which exists in an afterburning-engine tailpipe. The convergent nozzle and ejector was a 1/7.5-scale model of the exit of engine B of reference 5 (7,600 pounds static thrust at sea level). Complete details of the operation and characteristics of the turbojet simulator are given in reference 5.

Test and Procedure

The four afterbody configurations were tested over a range of Mach numbers from 0.80 to 1.10 at angles of attack from 0° to 5°. The Reynolds number, based on the wing mean aerodynamic chord, varied from 4.0×10^6 to 5.0×10^6. All configurations were tested at cruise operating conditions and afterbodies B and D in simulated afterburner operation. Data points were taken at primary jet total-pressure ratios of about 1, 2, 3, 4, 5, 7, and sometimes 9 (a pressure ratio of 1 indicates jet off), and each pressure ratio was held constant until the pressures and temperatures stabilized. All pressures were measured by using electrical pressure transducers, and the data were obtained on recording oscillographs.

Secondary air was supplied to the ejector through a small nose inlet. In order to simulate the secondary flow required for the engine in the nonafterburner condition, a choking restriction, sized to give

scaled secondary flow, was located in the nose inlet. A larger restric-
tion was used for the afterburner-on condition. The value of the
secondary-air weight flow was computed for each test point by using the
total and static pressure and stagnation temperature measured in the
throat of this restriction. Static pressure and stagnation temperature
were also measured at the exit of the secondary-air annulus.

Primary jet weight flow was measured by using a vane-type flowmeter
located in the hydrogen peroxide supply line. Primary jet total and
static pressures and stagnation temperature were measured just ahead of
the primary jet exit.

The afterbody drag coefficients presented are the results of inte-
grating the afterbody and base pressures from model station 55 (fig. 2)
to the base and across the base annulus (where existing) to the secondary-
air ejector and are based on the nominal wing area (4.44 square feet).
It should be noted that this afterbody drag is not for the complete air-
plane afterbody and that the results are particularly applicable only to
these afterbodies. It is also assumed that all the jet effects were
experienced over that portion of the afterbody which was included in the
pressure integrations. In integrating the pressures to obtain afterbody
drag, it was also assumed that the pressures located on each side of the
tail surfaces were effective to the chord line of the tail. The base
drag coefficients presented are the integration of the pressures over
the base annulus to the secondary-air ejector. Pressures were measured
over the skeg (tail hook and bumper fairing) and over a faired plate
with skeg off to evaluate the skeg pressure drag. Any pressure forces
in the secondary-air system are charged to the thrust system and are not
included in the afterbody drag integration.

Accuracy

A table of the estimated overall accuracy for the indicated param-
eters is presented as follows:

α, deg . . . . ± 0.1

M_∞ . . . . ± 0.005

C_D . . . . ± 0.0005

C_p . . . . ± 0.01

$p_{t,j}/p_\infty$ . . . . ± 0.1

$\dfrac{W_s}{W_p}\sqrt{\dfrac{T_s}{T_p}}$ . . . . ± 0.01

RESULTS

The results of the investigation are presented graphically as the variation of pressure coefficient over the afterbody and as afterbody and base drag coefficient with primary jet total-pressure ratio, Mach number, and angle of attack.

Examples of pressure-coefficient variation over the afterbodies are shown in figures 5 to 10. Only the results obtained at Mach numbers of 0.92 and 1.05 are presented for afterbodies A, B, and C. In general, the effects of the primary and secondary flows on the pressure distributions shown are typical of the effects at other Mach numbers in the subsonic and supersonic speed ranges. The variation of pressure coefficient over afterbody D is shown at all Mach numbers, angles of attack, and primary jet total-pressure ratios of the investigation. Presented in figure 11 is the variation of base pressure coefficient around the base annulus of afterbody D (afterburning and nonafterburning nozzles) at a primary jet total-pressure ratio of 1 (jet off) and 5 for several Mach numbers. It should be noted that any values of C_p plotted at $l/d_j = 0$ were measured on the base.

The corrected secondary weight-flow ratio $\frac{W_s}{W_p}\sqrt{\frac{T_s}{T_p}}$ varied with Mach number as well as with jet pressure ratio and is presented in figure 12 at several values of primary jet total-pressure ratio for each of the afterbody configurations tested.

The effect of jet total-pressure ratio on afterbody drag coefficient is shown in figure 13 for all afterbodies tested. The results are presented at $M = 0.80$ which is typical for all subsonic speeds and at $M = 1.09$ which is believed to be typical for low supersonic speeds. The variation of the afterbody and base drag coefficients with Mach number (jet off and nonafterburning nozzle) is presented in figure 14(a). Figures 14(b) and 14(c) present the base- and afterbody-drag-coefficient variations (nonafterburning nozzle), respectively, with Mach number for several values of primary jet total-pressure ratio, including jet off. The drag-coefficient variation with Mach number for the two afterbodies (B and D) tested with afterburning nozzles is shown in figure 15.

Results presented in figure 16 indicate the effect of the skeg on the drag coefficient of afterbody B. Figure 17 shows the effect, on afterbody drag, of extending the wing-tip fairings about 2 feet forward. Shadowgraphs taken with the two different fairings installed are shown in figure 18. The effect of tail interference on the afterbody drag coefficients of afterbodies A and D are shown in figure 19. Figure 20

shows the variation of drag coefficient with Mach number for afterbody B at angles of attack of $0°$ and $5°$ and at several values of primary jet total-pressure ratio.

DISCUSSION

Evaluation of Support Interference

The support system used would be expected to have little effect on the flow in the vicinity of the jet exits except at speeds where shock and expansion waves from the tips of the support booms can affect the pressure level and boundary-layer characteristics of the body. The tips of the support booms were tested in two positions with afterbody A to check these effects. (See figs. 2 and 4.) As shown in figure 17, forward movements of the tips of the support booms did cause measurable decreases in the overall afterbody and base drags above a Mach number of about 0.95. Shadowgraphs of the flow at pertinent operating conditions (fig. 18) show numerous pressure disturbances of the types generally encountered in transonic flows; however, there does not appear to be any significant change in the wave patterns traceable to changes in the position of the tips of the support booms. Comparison of representative afterbody pressure distributions for the two cases (figs. 5(b) and 5(c)) also does not disclose any significant flow changes (abrupt pressure change or separations) such as would be expected to accompany major changes in the pattern of waves reflecting from the tunnel walls and impinging on the afterbody. Instead, the changes in drag seem to be caused primarily by small, nearly uniform, increases in the level of pressures on the afterbody. In other words, it appears that support interference affects the present results mainly after the fashion of a buoyancy effect. It is concluded that, although the absolute values of pressure and drag coefficient may be subject to some slight error due to support interference, drag comparisons and jet-effects data shown are valid.

Several afterbody pressure-drag coefficients determined from pressure measurements made on the flight-test airplane are noted in figures 14(c) and 15. The engine total-pressure ratios corresponding to these data are believed to have been from 2.5 to 4 at subsonic speeds and 4.2 to 5 at supersonic speeds. The agreement of these drag coefficients with the model data is very good.

Afterbody-Pressure-Distribution Characteristics

Nonafterburning comparison of afterbodies A and B.- The effect on the pressure coefficients over afterbodies A and B of decreasing the

boattail angle by increasing the base area is seen in figures 5(a) and 6(a) for the subsonic speed range. It should be noted that after-body A has no physical base annulus (see fig. 3), but the small clearance area between the afterbody and secondary-air shroud is considered to be base area. Little change is seen in the pressure coefficients over the forward portion of afterbody B, but the base and rearmost afterbody pressure coefficients have been slightly reduced below those of A. The effect of increasing the jet pressure ratio was to aspirate the base region to lower pressure coefficients in both cases. At $M = 1.05$, afterbody A (fig. 5(b)) showed about the same pressure distribution as B (fig. 6(b)), but as the jet pressure ratio was increased, larger jet effects were seen on A (note C_p at $l/d_j = -0.44$).

The expected detrimental effect of the large boattail angle on afterbody A (average $\beta = 55^\circ$) was not shown in these data as it was in the isolated body tests of references 2 and 3. It is believed that the similarity of the pressure distribution over afterbodies A and B is the result of beneficial tail interference on A. This will be illustrated more clearly in the discussion of afterbody drag. Such interference effects are indicated in the results of reference 7 for low-fineness-ratio bodies with steep boattails.

Afterburning operation on afterbody B.- The effect of increasing the nozzle diameter to simulate afterburning condition on the afterbody pressures of B is shown by comparing the data in figures 6 and 7. In general, the afterbody and base pressures increased with increasing primary jet total-pressure ratio indicating more favorable jet effects for the afterburning nozzle. This trend is consistent with the results of previous investigations on isolated bodies.

Nonafterburning operation on afterbody C.- In figure 8(a) it is seen that further decreasing the effective boattail angle by lengthening the afterbody and, at the same time, reducing the base area caused the pressures over the rear and base of afterbody C to become positive and the jet effects to become beneficial at subsonic speeds. At $M = 1.05$ (fig. 8(b)) all pressure coefficients are reduced to negative values but again become more positive as the primary jet total-pressure ratio is increased. It should be noted that reference 8 indicates that the net change in pressures over the afterbody with a change in tail inci-dence from -1.5° to -4° is small.

Nonafterburning operation on afterbody D.- Comparison of figure 9(b) with 8(a) shows the change in pressure-coefficient distribution for afterbody D that resulted when the boattail angle was further reduced over that for afterbody C by increasing the base area. The major changes are seen to be an increase in pressure over the forward portion of the

afterbody, a reduction of the pressures over the rear of the afterbody
and base, and more adverse jet effects on the base pressures. Comparison
of afterbody D with C at M = 1.05 indicates the same changes in pres-
sures as were seen at M = 0.92.

Afterburning operation on afterbody D.- Pressure distributions on
afterbody D with the nozzle diameter increased to simulate afterburning
conditions are shown in figure 10. Comparison of the results shown in
figures 10(b) and 9(b) shows that, in general, the pressure coefficients
at M = 0.92 have been increased by increasing the nozzle diameter. The
same effects are seen at M = 1.05 in comparing figures 10(c) and 9(d).

Peripheral variation in pressure distributions.- The presence of the
horizontal and vertical tails and the asymmetry of the fuselage explains
the wide variance in pressure distributions shown around the afterbody
and base in figures 5 to 11. For example, the pressure distributions at
$\emptyset = 230^{\circ}$, which is just under the horizontal tail, follow rather closely
the expected pressure distribution on the airfoil surface. The base
pressure coefficients are very similar to the rearmost pressure coeffi-
cients on the afterbody, and the variation in base pressure coefficient
around the base (for example, fig. 11) indicates the necessity for
measuring pressures at several points on airplane models. It is noted
that the differences in the jet-off base pressure coefficients with the
afterburning and nonafterburning nozzles is the result of increased
secondary-air flow with the former condition.

Drag Characteristics

Effect of jet total-pressure ratio.- Figure 13 shows the effect of
jet total-pressure ratio on the drag coefficients of all the afterbodies
at two Mach numbers selected as being typical of the subsonic and low
supersonic speed ranges. The jet effects of all configurations were
generally similar to those shown previously for isolated bodies in that
the drag coefficients increased through a range of pressure ratios and
finally decreased again at still higher pressure ratios. The jet total-
pressure ratios at which these changes in drag coefficient occurred were
a function primarily of the ratio of exit diameter to base diameter.
(Note the early beneficial effect on afterbody C.)

When studying the drag characteristics shown in figures 14 and 15,
it should be remembered that all afterbodies except afterbody A are
equipped with an arresting hook fairing and that afterbody C was inves-
tigated with only an angle of incidence of -4° of the horizontal tail,
compared with a tail-incidence angle of -1.5° for the other configura-
tions. The drag increment due to the skeg is shown in figure 16, and
the effect of tail incidence has been discussed in a previous section.

Aside from these differences, the drag coefficients of these configurations varied with Mach number and jet pressure ratio generally in the same manner as the drag coefficients of isolated bodies studied in other investigations (refs. 1 to 4).

At pressure ratios and nozzle settings typical for current turbojet engines $\left(p_{t,j}/p_\infty = 2.5 - 5.5\right)$, afterbody D had the lowest drag throughout the Mach number range for both afterburning and nonafterburning jet operation. This occurrence was in spite of the appreciable base drag, which amounted to about 6 percent of the estimated zero-lift drag of the airplane in the cruise operating condition. A study of the drag characteristics of afterbodies C and D will reveal the possibility of an afterbody with less base area than D and lower boattail angles than C (with average $\beta = 8^{\circ}$) that should have better drag characteristics than either C or D.

Effect of tail interferences.- The interference effects caused large and sometimes unexpected changes in the relative merits of the several afterbodies. For example, in the case of the short afterbodies A and B, where the boattail angle was decreased by increasing the base area, the afterbody drag of B did not decrease appreciably from that of A. This unexpected result was estimated to be due to tail interference. In order to indicate the magnitude of the tail interference and other interferences on the afterbodies, drag coefficients have been determined for symmetrical afterbodies (no tails) by extrapolating the data in references 3 and 4 to values of l/d_m and d_b/d_m corresponding to afterbodies A and D.

These drag coefficients are presented in figure 19 along with the drag coefficients obtained on afterbodies A and D at Mach numbers of 0.90 and 1.10 and at a pressure ratio of 3.0. The drag coefficients from the reference data are based on an area determined from the ratio of the wing area to the fuselage cross-sectional area of the airplane model. For the parabolic afterbody with a large boattail angle (afterbody A), the effect of the tail and other interferences at $M = 0.90$ was to reduce the drag coefficient from 0.0150 to 0.0030, and at $M = 1.10$ from 0.0310 to 0.0070. However, on afterbody D it can be seen that at $M = 0.90$ the drag coefficient has increased (0.0009 to 0.0023) 150 percent, whereas at $M = 1.10$ there is little change in drag. When the horizontal tails were removed, the drag coefficient of D at $M = 0.90$ was 0.0014; that is, about 33 percent of the drag increase was due to the vertical tail. This indicates that the effect of each of the tails is about the same and, in addition, there is little or no change in the afterbody pressure drag due to the small angle of incidence (-1.5°) of the horizontal tail.

An interesting item is that, although there was no decrease in tail interference with Mach number on afterbody A, there was a decrease in

tail interference with increasing Mach number on afterbody D. It should
be pointed out that the drag coefficients given for the afterbodies cor-
responding to afterbodies A and D were obtained by extrapolation and,
therefore, the absolute value of drag coefficient due to tail interfer-
ence may be subject to some error. However, it is felt that it has been
established that, for this investigation, there were large changes in
afterbody drag due to tail interference and that the tail interference
must be considered when estimating the afterbody performance.

Effect of angle of attack.- The results of figure 20 show that the
drag characteristics of afterbody B are relatively unchanged with angle
of attack up to 5°. These results are typical for all the other
afterbodies.

CONCLUSIONS

An investigation of the effects of a hot-jet exhaust on several
afterbody shapes of a single-engine fighter-airplane model has been
conducted in the Langley 16-foot transonic tunnel at Mach numbers from
0.80 to 1.10 and angles of attack from 0° to 5°. The afterbody-geometry
variables were boattail angle, afterbody length, and base area. The
primary jet total-pressure ratio was varied from 1 (jet off) to 7 for
primary jet diameters corresponding to afterburning and nonafterburning
nozzles. The results of the investigation indicate the following
conclusions:

1. The pressure distributions on the afterbodies and bases varied
widely from that of symmetrical bodies because of the asymmetry of the
fuselage and the presence of tail surfaces.

2. Tail-interference effects were variable for the different after-
bodies. They were large and beneficial on an afterbody with large
boattail angles (afterbody A) and small and detrimental on an afterbody
with low boattail angles (afterbody D).

3. In general, the afterbody drag coefficients varied in the same
manner as the drag of isolated afterbodies; namely, the drag was reduced
by increasing afterbody length, increasing jet diameter, and decreasing
boattail angle, despite a resulting increase in base area.

4. The measured pressure drag of the afterbody with the lowest
boattail angles (afterbody D) is better than that of all other configura-
tions investigated for typical turbojet-engine pressure ratios, even
though afterbody D experienced large detrimental jet effects.

5. In general, the jet effects on the afterbodies were similar to those shown previously for isolated symmetrical afterbodies in that the drag coefficient decreased, increased, and decreased again as the pressure-ratio range was traversed. The pressure ratios at which these changes occurred were a function primarily of the ratio of exit diameter to base diameter.

Langley Aeronautical Laboratory,
    National Advisory Committee for Aeronautics,
        Langley Field, Va., September 19, 1957.

REFERENCES

1. Salmi, Reino J.: Experimental Investigation of Drag of Afterbodies With Exiting Jet at High Subsonic Mach Numbers. NACA RM E54I13, 1954.

2. Henry, Beverly Z., Jr., and Cahn, Maurice S.: Pressure Distributions Over a Series of Related Afterbody Shapes As Affected by a Propulsive Jet at Transonic Speeds. NACA RM L56K05, 1957.

3. Henry, Beverly Z., Jr., and Cahn, Maurice S.: Preliminary Results of an Investigation at Transonic Speeds To Determine the Effects of a Heated Propulsive Jet on the Drag Characteristics of a Related Series of Afterbodies. NACA RM L55A24a, 1955.

4. Cubbage, James M., Jr.: Jet Effects on the Drag of Conical Afterbodies for Mach Numbers of 0.6 to 1.28. NACA RM L57B21, 1957.

5. Runckel, Jack F., and Swihart, John M.: A Hydrogen Peroxide Turbojet-Engine Simulator for Wind-Tunnel Powered-Model Investigations. NACA RM L57H15, 1957.

6. Ward, Vernon G., Whitcomb, Charles F., and Pearson, Merwin D.: Air-Flow and Power Characteristics of the Langley 16-Foot Transonic Tunnel With Slotted Test Section. NACA RM L52E01, 1952.

7. Stoney, William E., Jr.: Some Experimental Effects of Afterbody Shape on the Zero-Lift Drag of Bodies for Mach Numbers Between 0.80 and 1.3. NACA RM L53I01, 1953.

8. Valerino, Alfred S.: Jet Effects on Pressure Loading of All-Movable Horizontal Stabilizer. NACA RM E54C24, 1954.

TABLE I.- AFTERBODY PRESSURE-ORIFICE LOCATION

(a) Afterbody A

$\phi = 180^\circ$		$\phi = 215^\circ$		$\phi = 230^\circ$		$\phi = 290^\circ$		$\phi = 325^\circ$		$\phi = 352^\circ$	
l, in.	l/d_j	l, in.	l/d_j	l, in.	l/d_j	l, in.	l/d_j	l, in.	l/d_j	l, in.	l/d_j
-0.33	-0.127	-0.33	-0.127	-0.47	-0.179	-0.20	-0.076	-0.20	-0.076	-0.179	-0.179
-1.27	-.485	-1.27	-.485	-1.13	-.433	-.47	-.179	-1.13	-.433	-3.79	-1.453
-2.47	-.943	-2.47	-.943	-3.79	-1.453	-3.79	-1.453	-2.20	-.841	-5.66	-2.167
-3.79	-1.453			-5.66	-2.167	-5.66	-2.167				
-5.66	-2.167										

(b) Afterbody B

$\phi = 230^\circ$			$\phi = 285^\circ$			$\phi = 327^\circ$			$\phi = 352^\circ$		
l, in.	l/d_j	$l/d_{j,A/B}$	l, in.	l/d_j	$l/d_{j,A/B}$	l, in.	l/d_j	$l/d_{j,A/B}$	l, in.	l/d_j	$l/d_{j,A/B}$
0	0	0	0	0	0	0	0	0	(a)	(a)	(a)
-.33	-.127	-.101	-.33	-.127	-.101	-1.27	-.485	-.384	-0.33	-0.127	-0.101
-1.27	-.485		-3.79	(a)	-1.148	-2.47	-.943	-.745	-3.79	-1.453	-1.148
-2.47	-.943	-.745	-5.66	-2.167	-1.712				-5.66	-2.167	-1.712
-3.79	-1.453	-1.148									
-5.66	-2.167	-1.712									

[a] Orifice inoperative.

TABLE I.- AFTERBODY PRESSURE ORIFICE LOCATION - Concluded

(c) Afterbody C

$\phi = 215°$		$\phi = 230°$		$\phi = 294°$		$\phi = 330°$		$\phi = 352°$	
l, in.	l/d_j	l, in.	l/d_j	l, in.	l/d_j	l, in.	l/d_j	l, in.	l/d_j
-2.02	-0.773	-0.77	-0.296	-3.57	-1.366	-0.77	-0.296	-0.77	-0.296
		-2.11	-.806	-6.36	-2.437	-2.11	-.806	-6.36	-2.437
		-3.57	-1.366	-8.24	-3.151	-4.91	-1.876	-8.24	-3.151
		-4.91	-1.876						
		-6.32	-2.437						
		-8.24	-3.151						

(d) Afterbody D

$\phi = 180°$			$\phi = 200°$			$\phi = 220°$			$\phi = 280°$			$\phi = 326°$			$\phi = 352°$		
l, in.	l/d_j	$l/d_{j,A/B}$	l, in.	l/d_j	$l/d_{j,A/B}$	l, in.	l/d_j	$l/d_{j,A/B}$	l, in.	l/d_j	$l/d_{j,A/B}$	l, in.	l/d_j	$l/d_{j,A/B}$	l, in.	l/d_j	$l/d_{j,A/B}$
-1.36	-0.522	-0.412	-0.40	-0.153	-0.121	0	0	0	0	0	0	0	0	0	0	0	0
-5.04	-1.928	-1.523				-.40	-.153	-.121	-.40	-.153	-.121	-.40	-.153	-.121	-6.38	-2.438	-1.926
						-1.71	-.653	-.516	-1.71	-.653	-.516	-1.71	-.653	-.516	-8.24	-3.152	-2.490
						-4.48	-1.711	-1.352	-2.81	-1.074	-.848	-2.81	-1.074	-.848			
						-6.38	-2.438	-1.926	-6.38	-2.438	-1.926	-4.48	-1.711	-1.352			
						-8.24	-3.152	-2.49	-8.24	-3.152	-2.490						
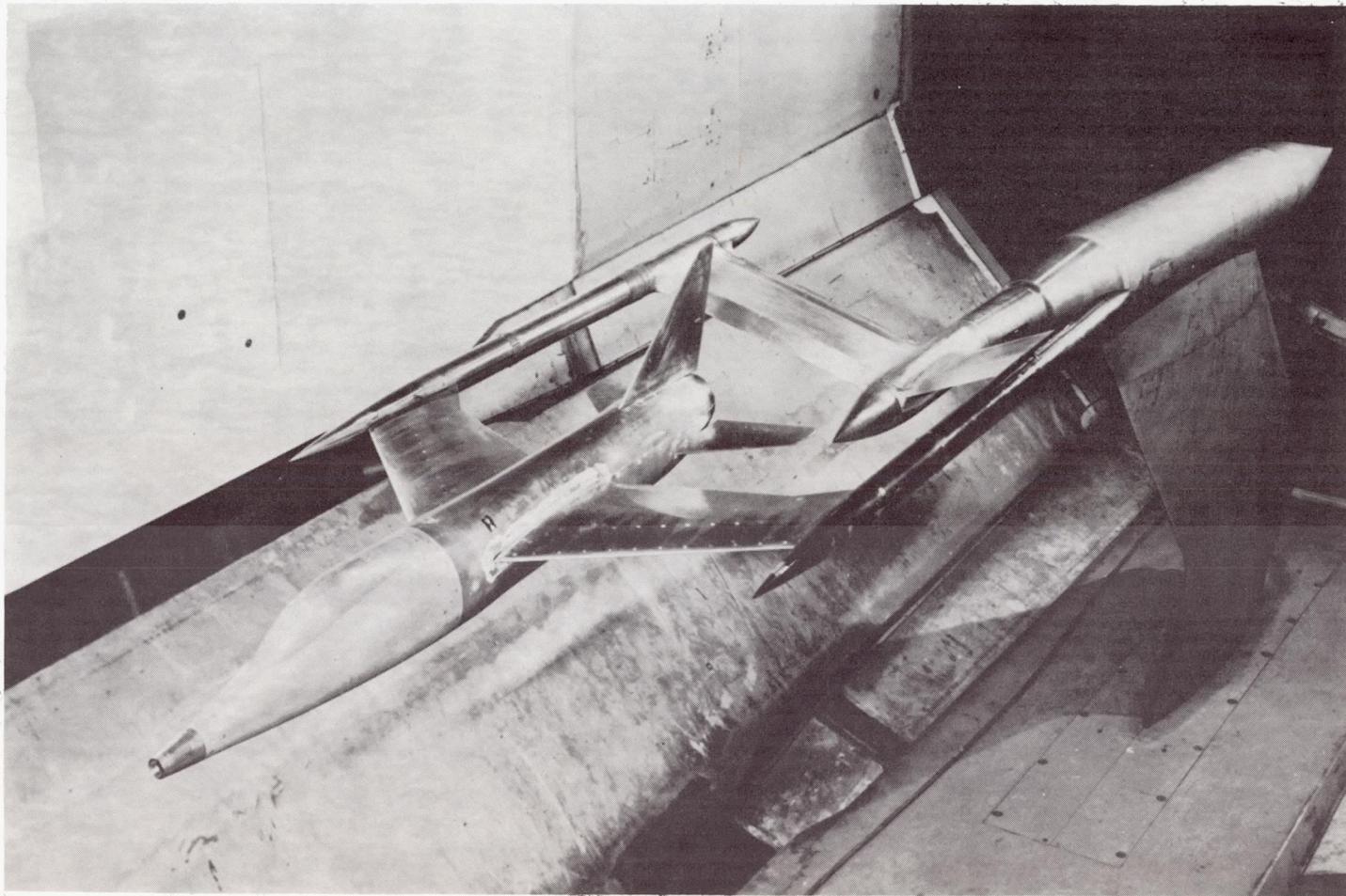
(a) Three-quarter front view.   L-92288

Figure 1.- Photograph of jet-exhaust simulator model with afterbody B in the Langley 16-foot transonic tunnel.
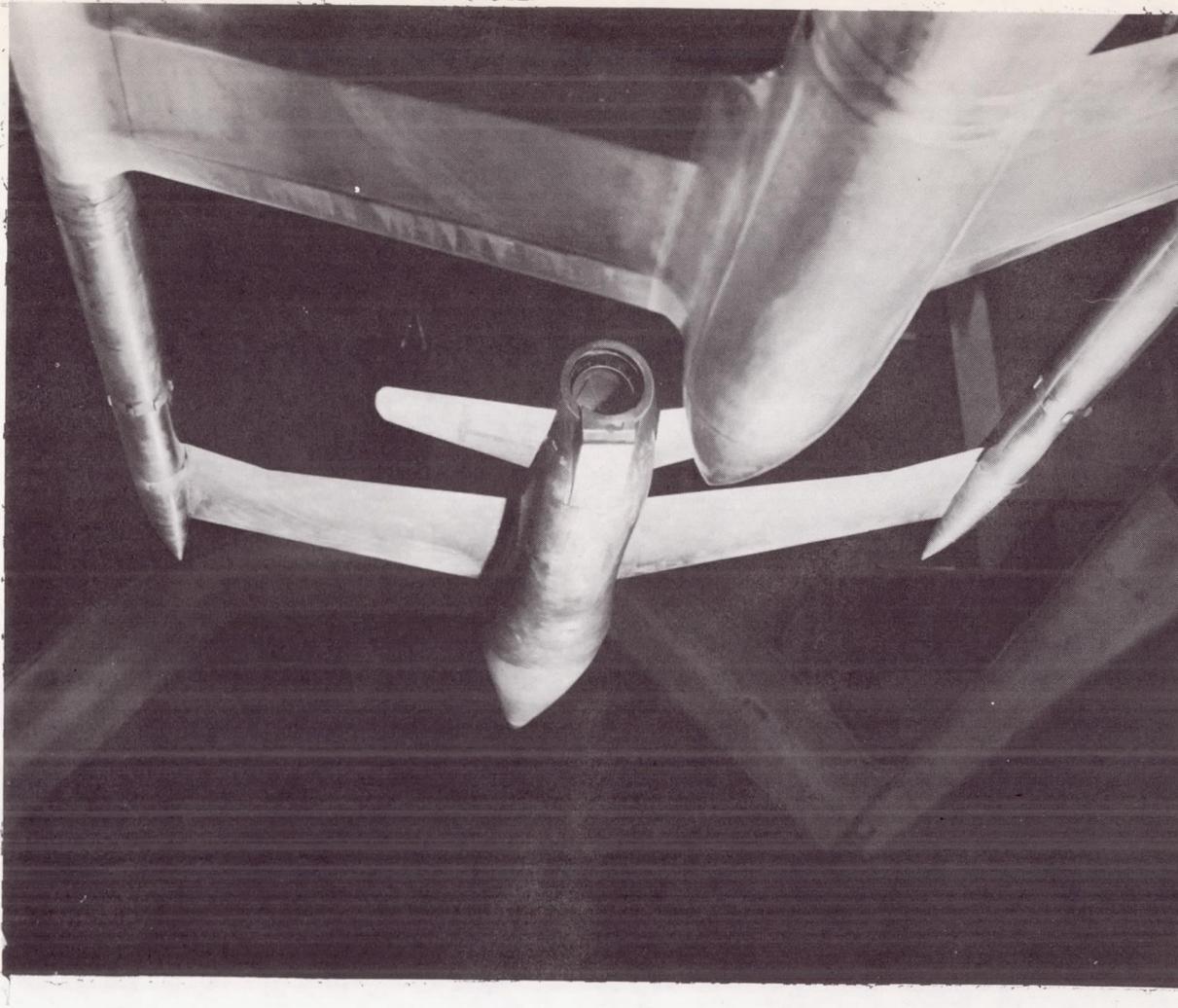
(b) Lower rear view of model with afterbody B.   L-92289

Figure 1.- Concluded.
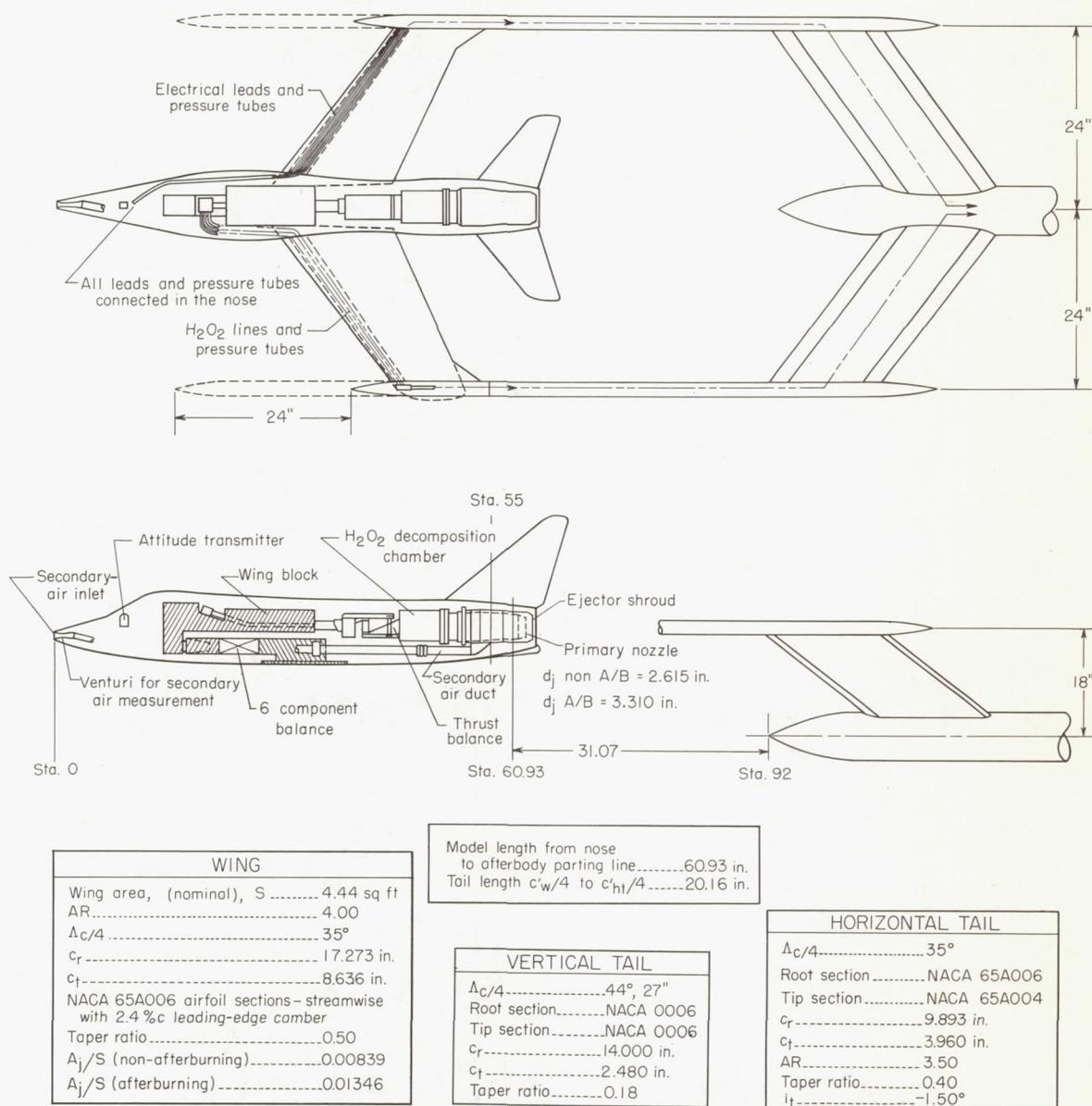
Figure 2.- Sketch of jet-exhaust simulator model and support system.

WING	
Wing area, (nominal), S	4.44 sq ft
AR	4.00
$\Lambda_{c/4}$	35°
c_r	17.273 in.
c_t	8.636 in.
NACA 65A006 airfoil sections – streamwise with 2.4% c leading-edge camber	
Taper ratio	0.50
A_j/S (non-afterburning)	0.00839
A_j/S (afterburning)	0.01346

Model length from nose to afterbody parting line _____ 60.93 in.
Tail length $c'_w/4$ to $c'_{ht}/4$ _____ 20.16 in.

VERTICAL TAIL	
$\Lambda_{c/4}$	44°, 27"
Root section	NACA 0006
Tip section	NACA 0006
c_r	14.000 in.
c_t	2.480 in.
Taper ratio	0.18

HORIZONTAL TAIL	
$\Lambda_{c/4}$	35°
Root section	NACA 65A006
Tip section	NACA 65A004
c_r	9.893 in.
c_t	3.960 in.
AR	3.50
Taper ratio	0.40
i_t	−1.50°

Trailing-edge tails

$\beta \approx 50° \rightarrow 60°$

$\phi = 242°$

$A_b = 0.0269$ ft^2

$\dfrac{d_j}{d_b} = 0.666$

$\dfrac{l_s}{d_j} = 0.50$

$\dfrac{l_a}{Z} = 0.91$

Afterbody A

$\phi = 0°$; $\beta = 13°$
$\phi \ \ 45°$; $\beta = 14.9°$
$\phi = 90°$; $\beta = 19°$
$\phi = 135°$; $\beta = 24.4°$
$\phi = 180°$; $\beta = 23°$
$A_b = 0.0350$ ft^2

$\dfrac{d_j}{d_b} = 0.523$

$\dfrac{l_s}{d_j} = 0.58$

$\dfrac{l_a}{Z} = 0.93$

Afterbody B

Tail hook and bumper fairing

$\phi = 0°$; $\beta = 10°$
$\phi = 45°$; $\beta = 11.5°$
$\phi = 90°$; $\beta = 12°$
$\phi = 135°$; $\beta = 16°$
$\phi = 180°$; $\beta = 15°$
$A_b = 0.0285$ ft^2

$\dfrac{d_j}{d_b} = 0.643$

$\dfrac{l_s}{d_j} = 0.48$

$\dfrac{l_a}{Z} = 1.17$

Afterbody C

$\phi = 0°$; $\beta = 4°$
$\phi = 45°$; $\beta = 5°$
$\phi = 90°$; $\beta = 5.6°$
$\phi = 135°$; $\beta = 8.4°$
$\phi = 180°$; $\beta = 11°$
$A_b = 0.0519$ ft^2

$\dfrac{d_j}{d_b} = 0.511$

$\dfrac{l_s}{d_j} = 0.48$

$\dfrac{l_a}{Z} = 1.17$

Afterbody D

(a) Afterbody physical characteristics and dimensions.

Figure 3.- Geometric characteristics and dimensions of afterbodies.

A

B

C

D
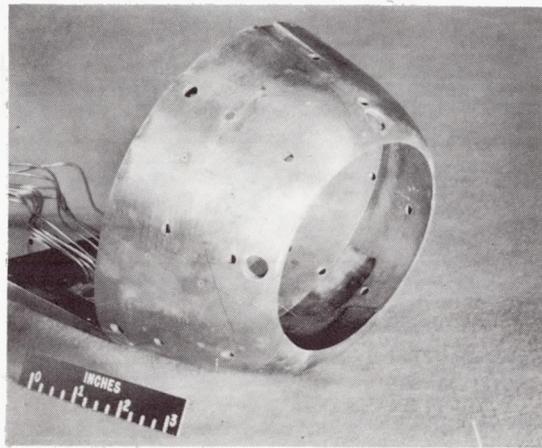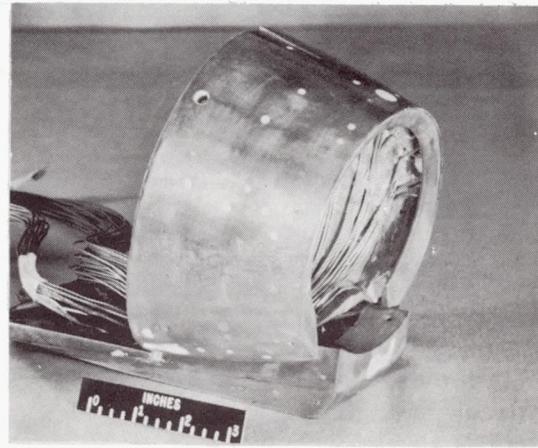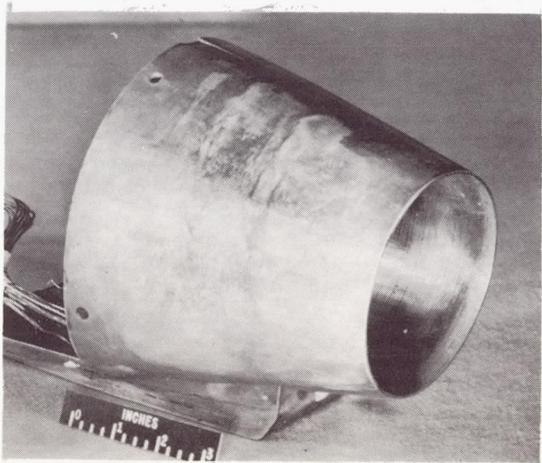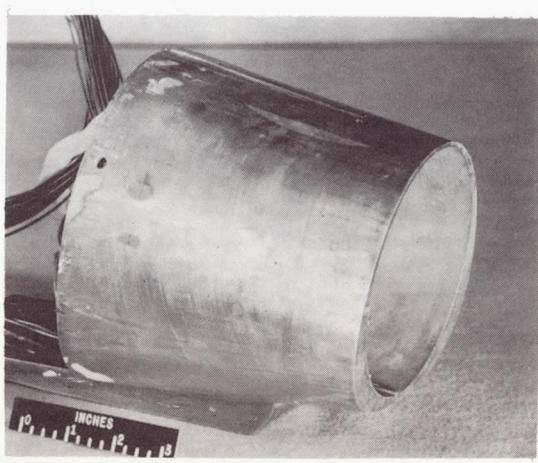
L-57-2763

(b) Photographs of afterbodies used in the investigation.

Figure 3.- Concluded.
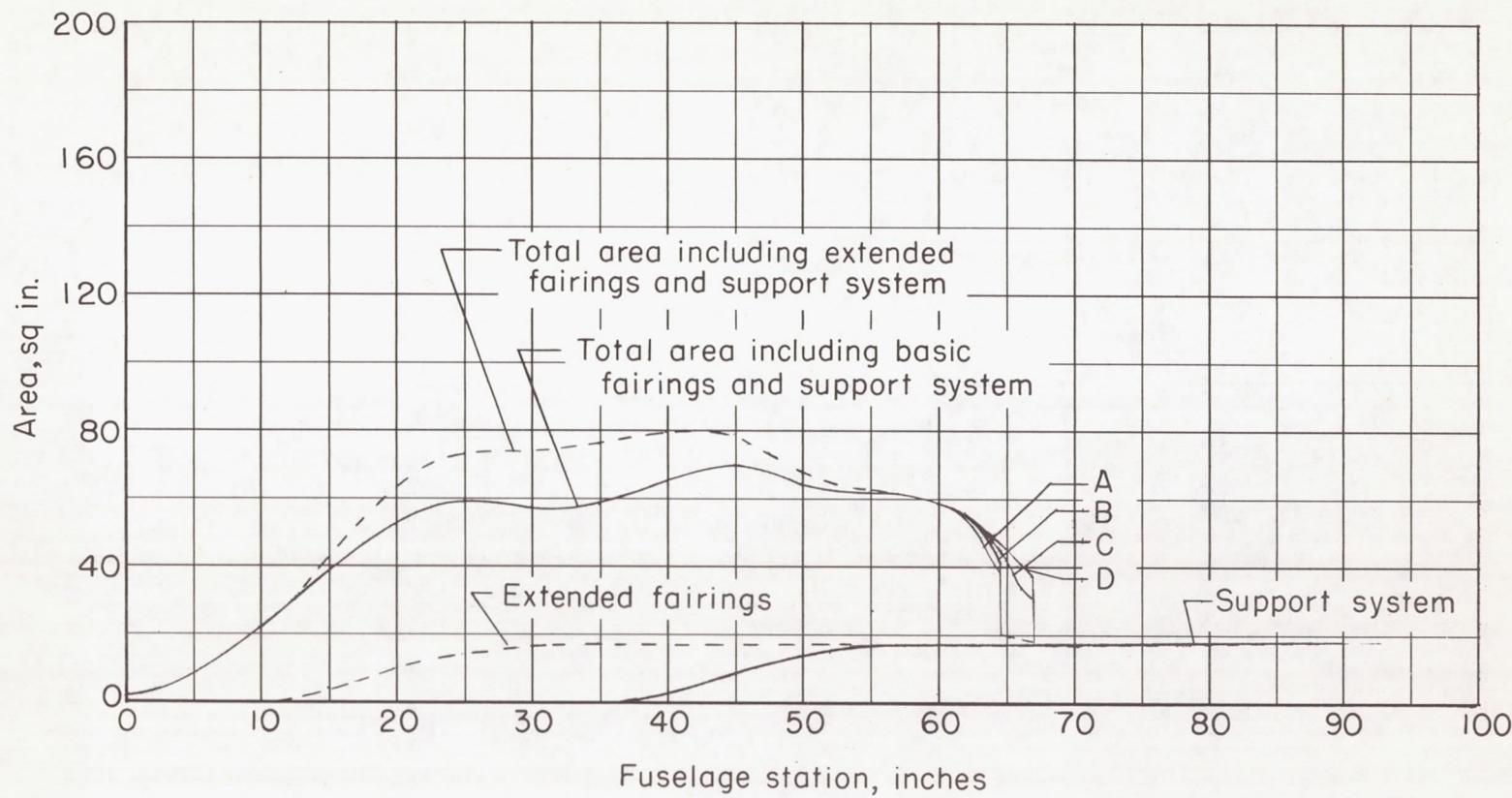
Figure 4.- Area development of airplane model and afterbodies tested, including the support system.
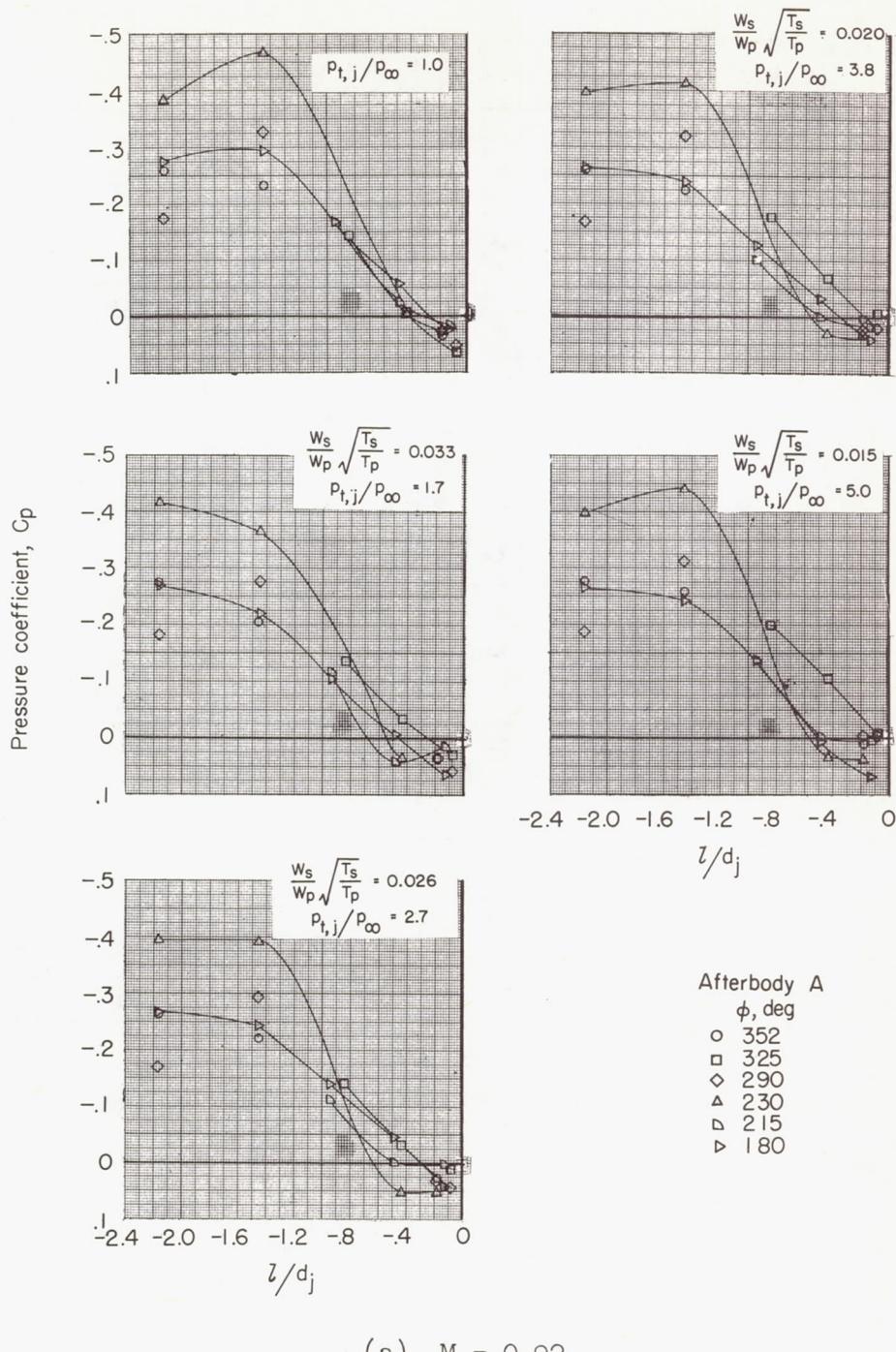
(a)   M = 0.92.

Figure 5.- Examples of pressure-coefficient variation over afterbody A.
$\alpha = 0^\circ$; $i_t = -1.5^\circ$; nonafterburning nozzle.
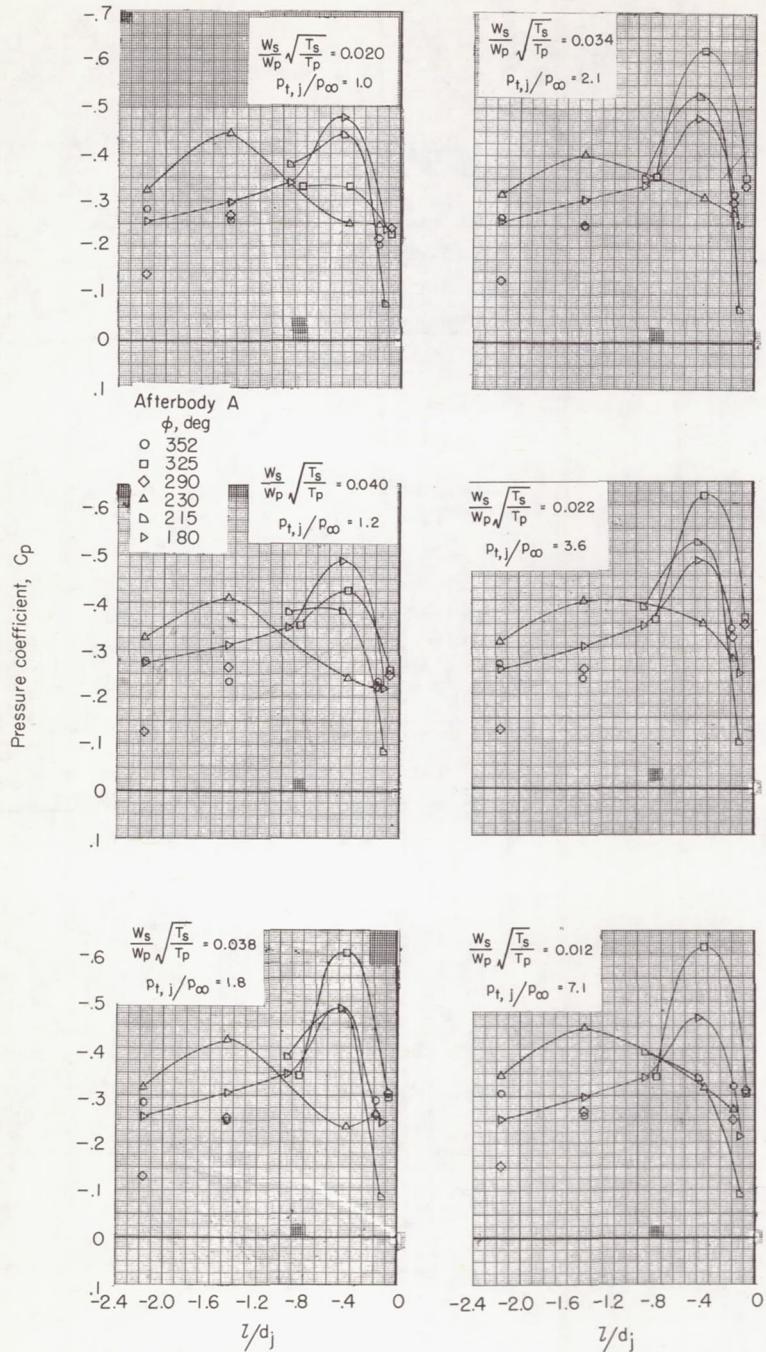
(b) M = 1.05.

Figure 5.- Continued.
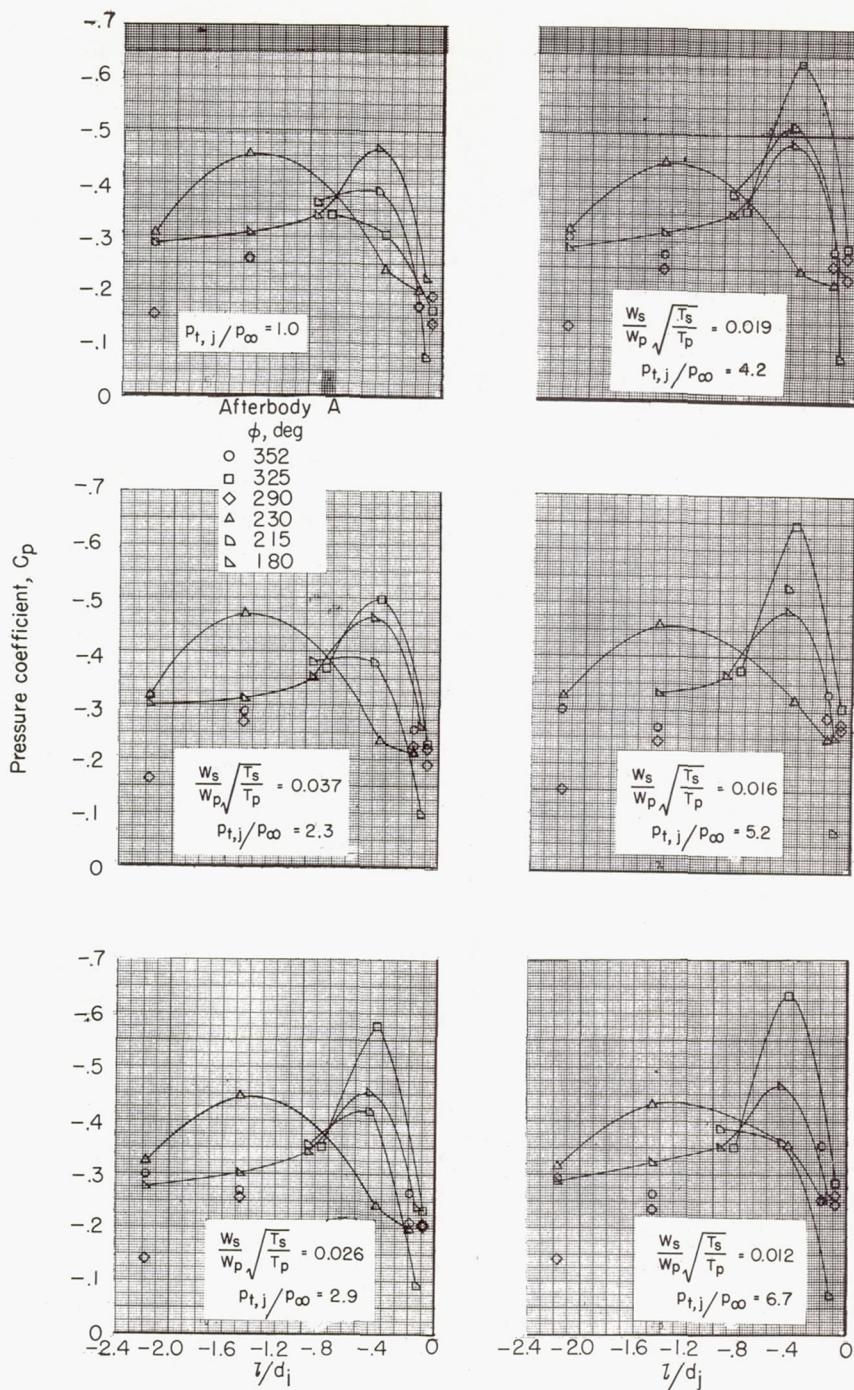
(c) Extended wing-tip fairings.

Figure 5.- Concluded.
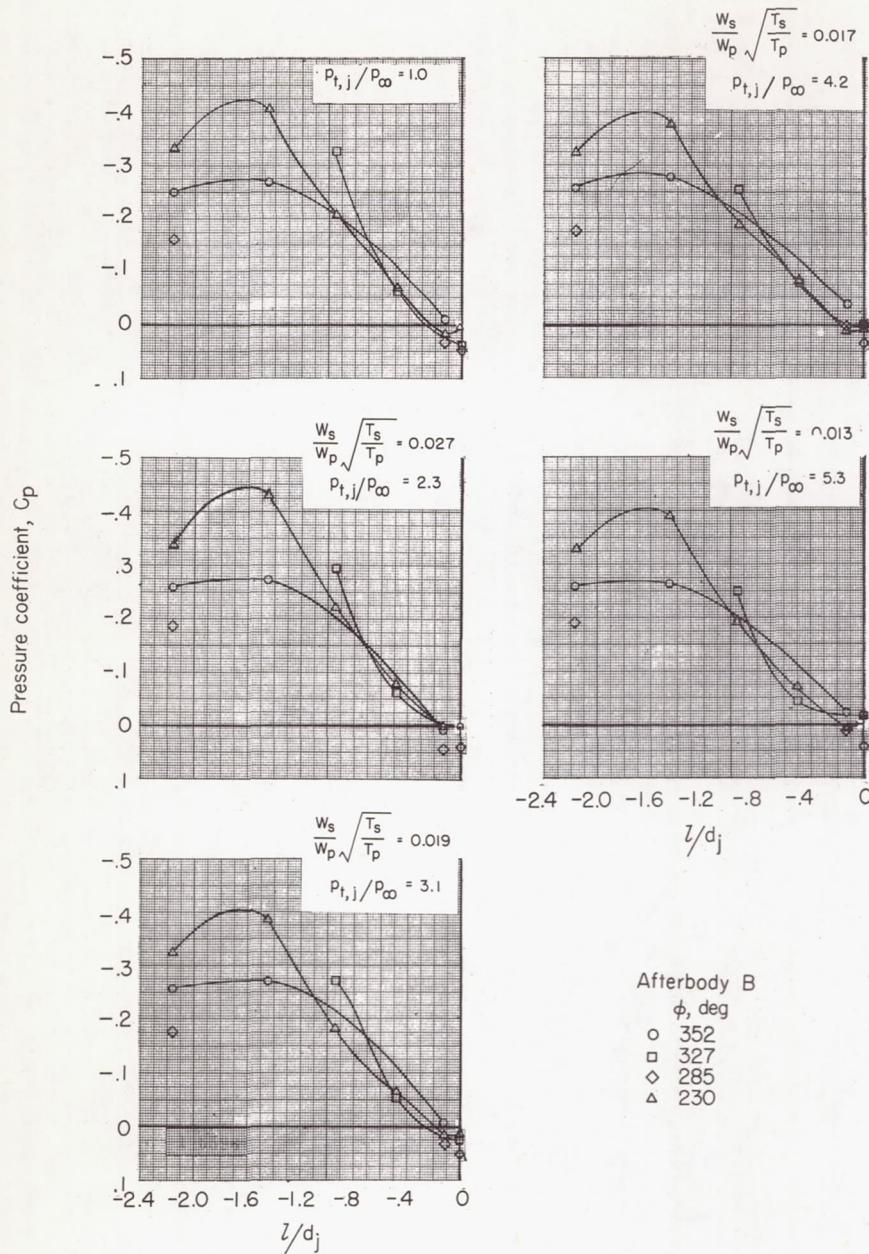
(a)   M = 0.92.

Figure 6.- Examples of pressure-coefficient variation over afterbody B.
$\alpha = 0^{\circ}$; $i_t = -1.5^{\circ}$; nonafterburning nozzle.
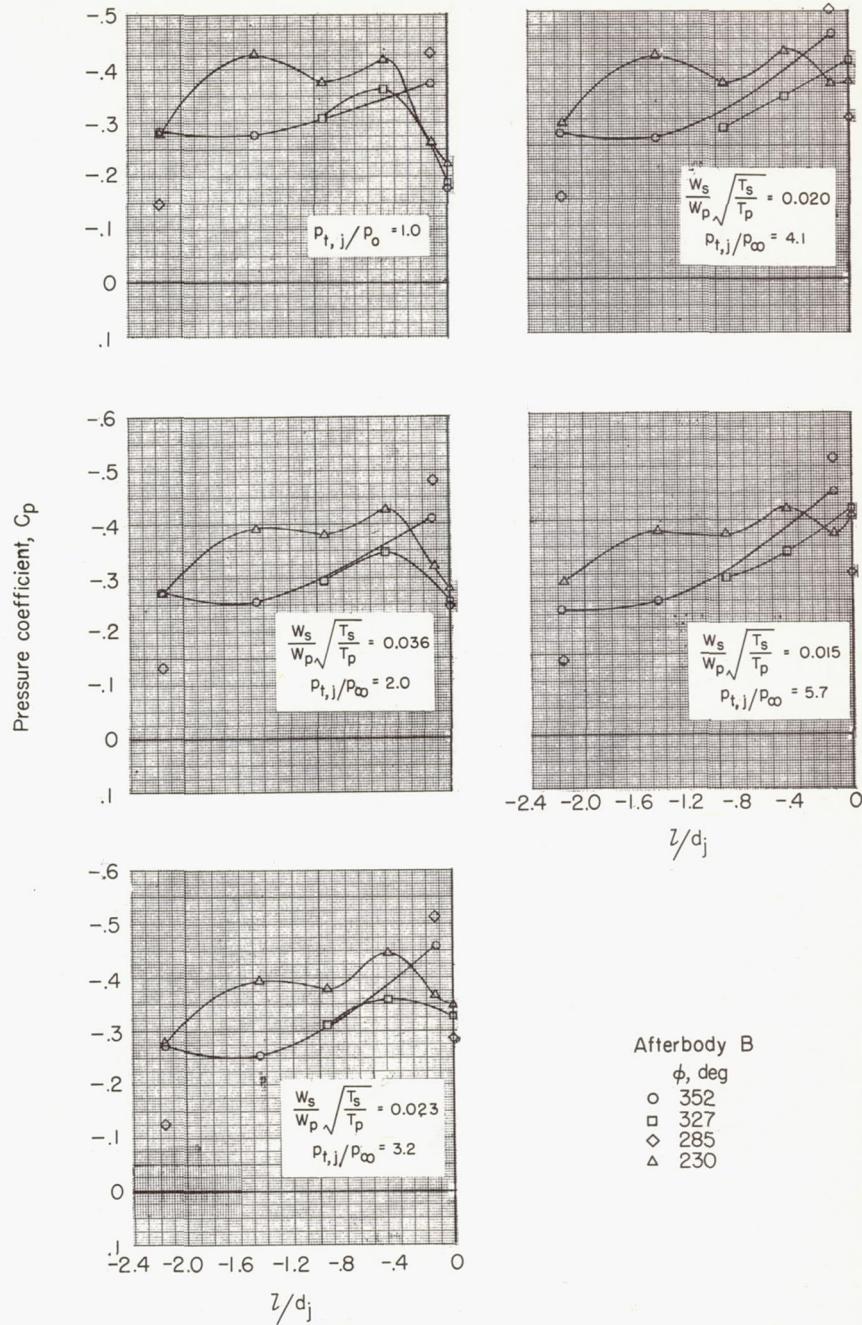
(b) M = 1.05.

Figure 6.- Concluded.
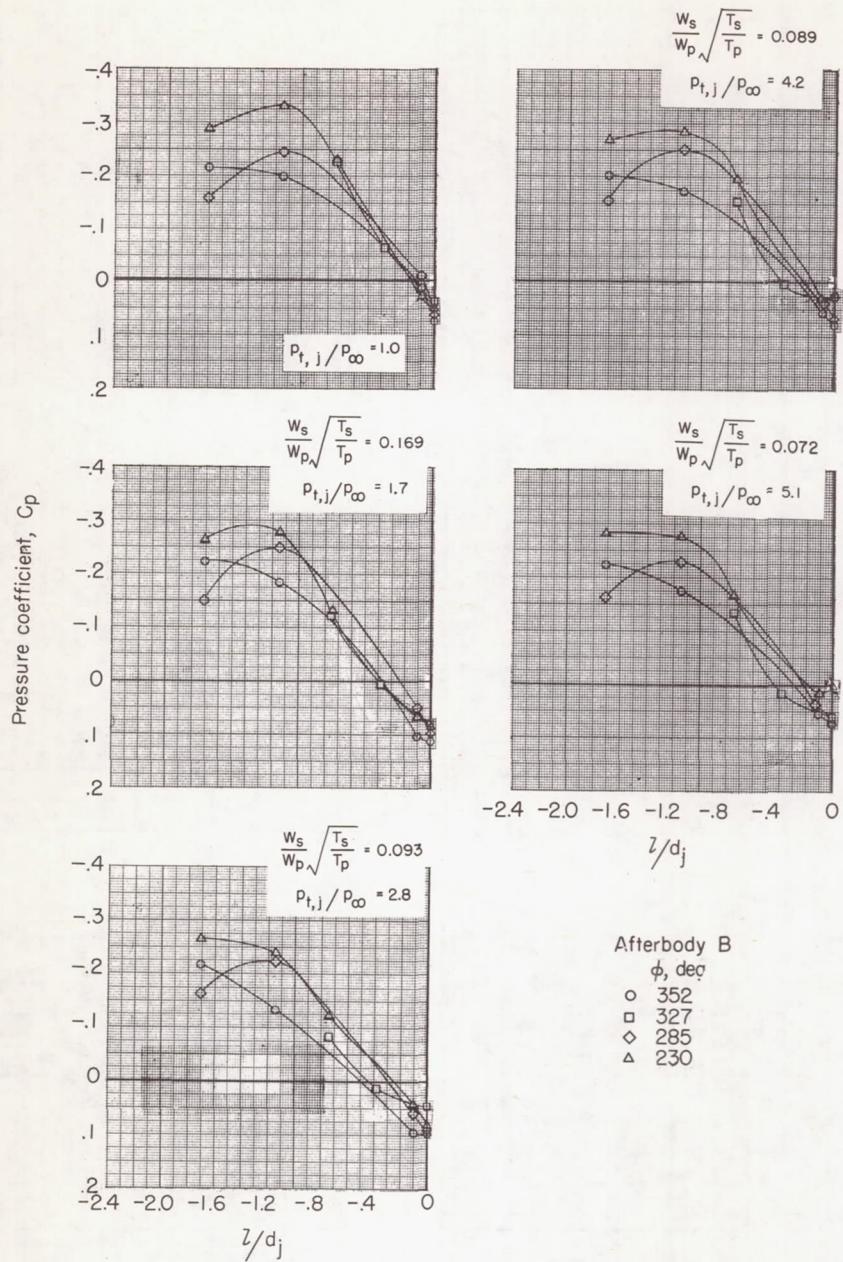
(a)   M = 0.92.

Figure 7.- Examples of pressure-coefficient variation over afterbody B.
$\alpha = 0^\circ$; $i_t = -1.5^\circ$; afterburning nozzle.
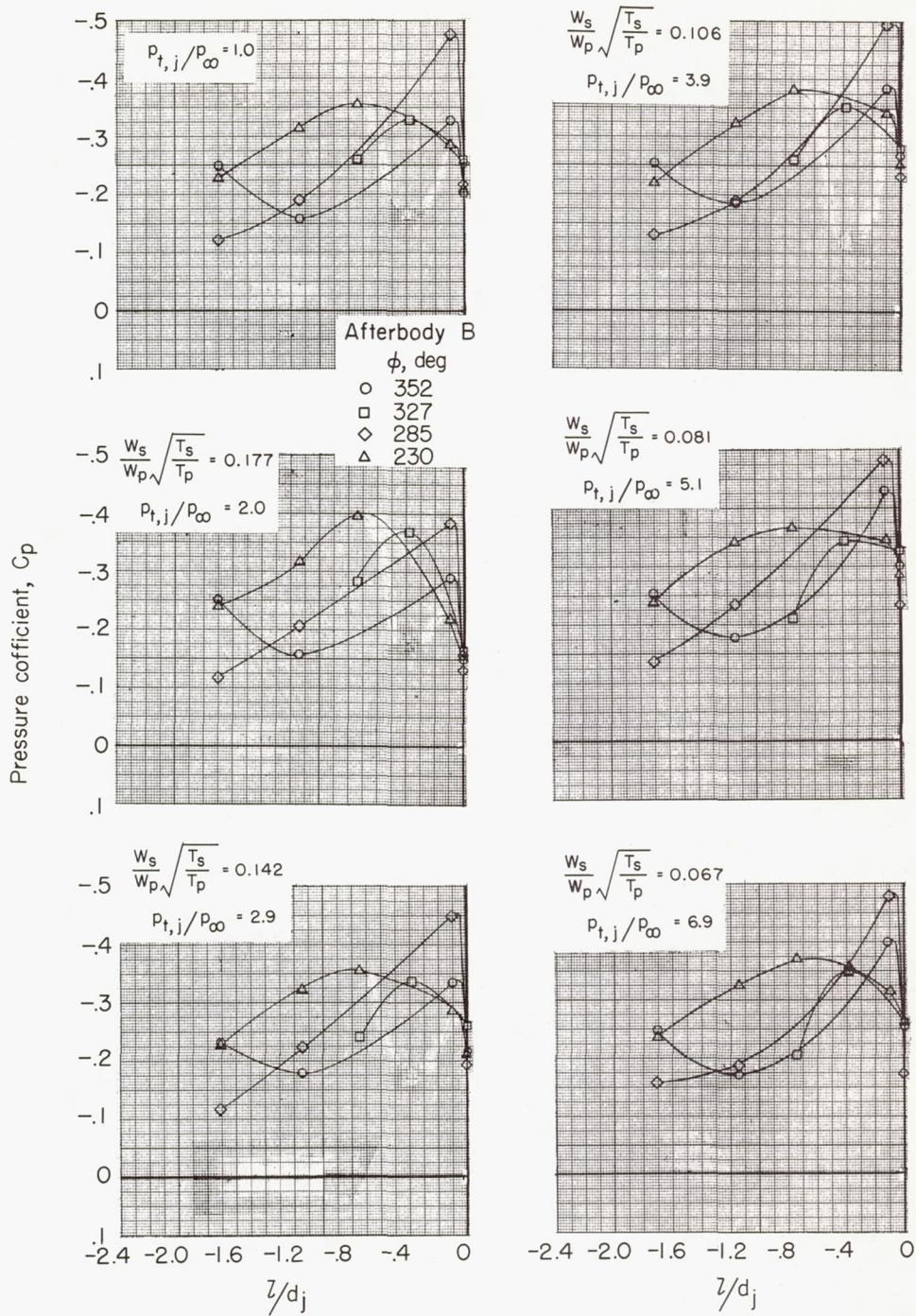
(b) M = 1.05.

Figure 7.- Concluded.

(a) M = 0.92.
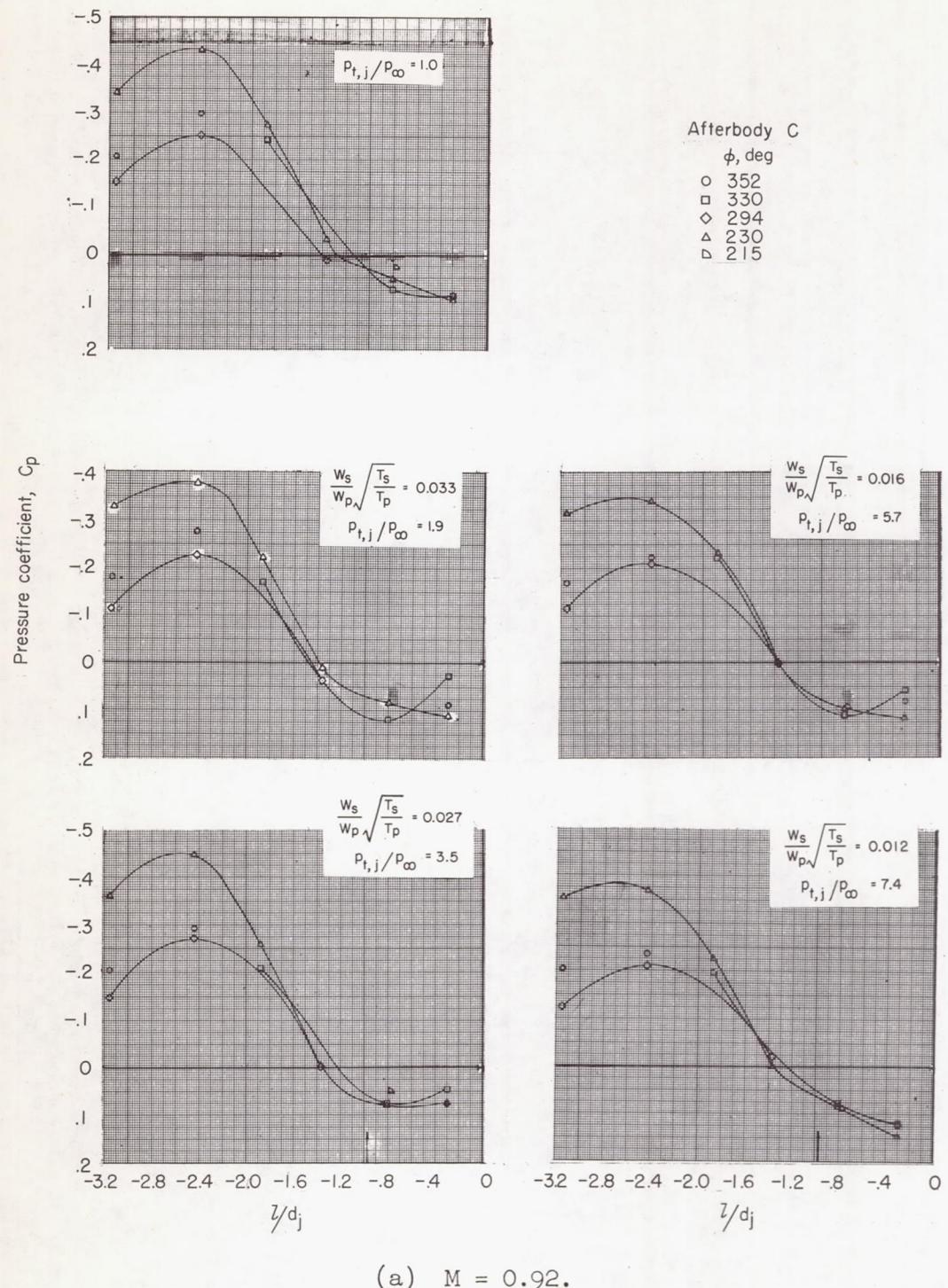
Figure 8.- Examples of pressure-coefficient variation over afterbody C.
α = 0°; i_t = -4°; nonafterburning nozzle.
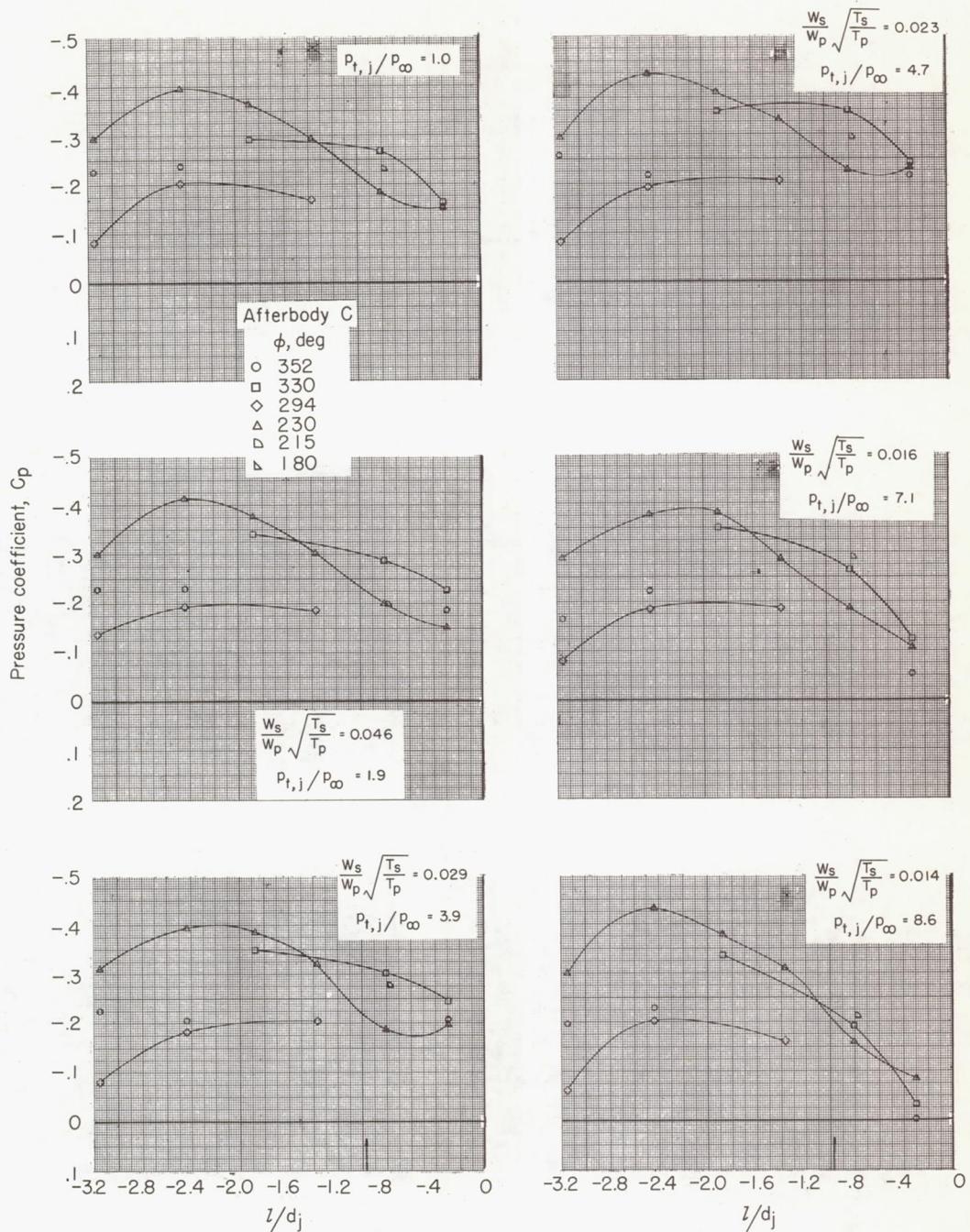
(b)   M = 1.05.

Figure 8.- Concluded.
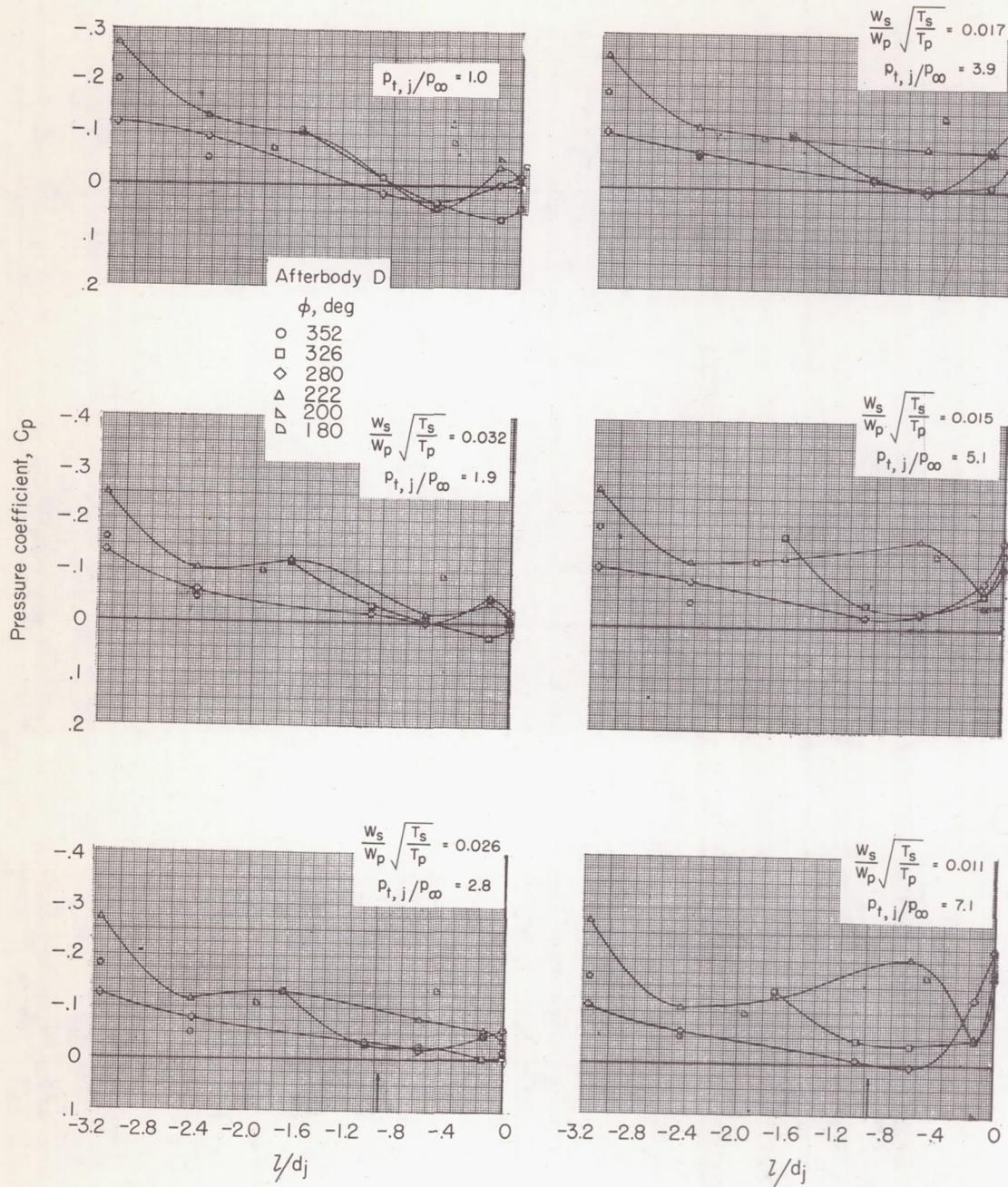
(a) M = 0.80; α = 0°.

Figure 9.- Pressure-coefficient variation over afterbody D. Nonafter-
burning nozzle; i_t = -1.5°.

(b) M = 0.92; α = 0°.

Figure 9.- Continued.

(c) M = 1.00; α = 0°.

Figure 9.- Continued.

Pressure coefficient, C_p

$p_{t,j}/p_\infty = 1.0$

$\dfrac{w_s}{w_p}\sqrt{\dfrac{T_s}{T_p}} = 0.018$

$p_{t,j}/p_\infty = 5.2$

Afterbody D

ϕ, deg
- ○ 352
- □ 326
- ◇ 280
- △ 222
- ⊿ 200
- ◁ 180

$\dfrac{w_s}{w_p}\sqrt{\dfrac{T_s}{T_p}} = 0.041$

$p_{t,j}/p_\infty = 1.8$

$\dfrac{w_s}{w_p}\sqrt{\dfrac{T_s}{T_p}} = 0.013$

$p_{t,j}/p_\infty = 7.2$

$\dfrac{w_s}{w_p}\sqrt{\dfrac{T_s}{T_p}} = 0.023$

$p_{t,j}/p_\infty = 4.1$

$\dfrac{w_s}{w_p}\sqrt{\dfrac{T_s}{T_p}} = 0.010$

$p_{t,j}/p_\infty = 8.6$

l/d_j

l/d_j
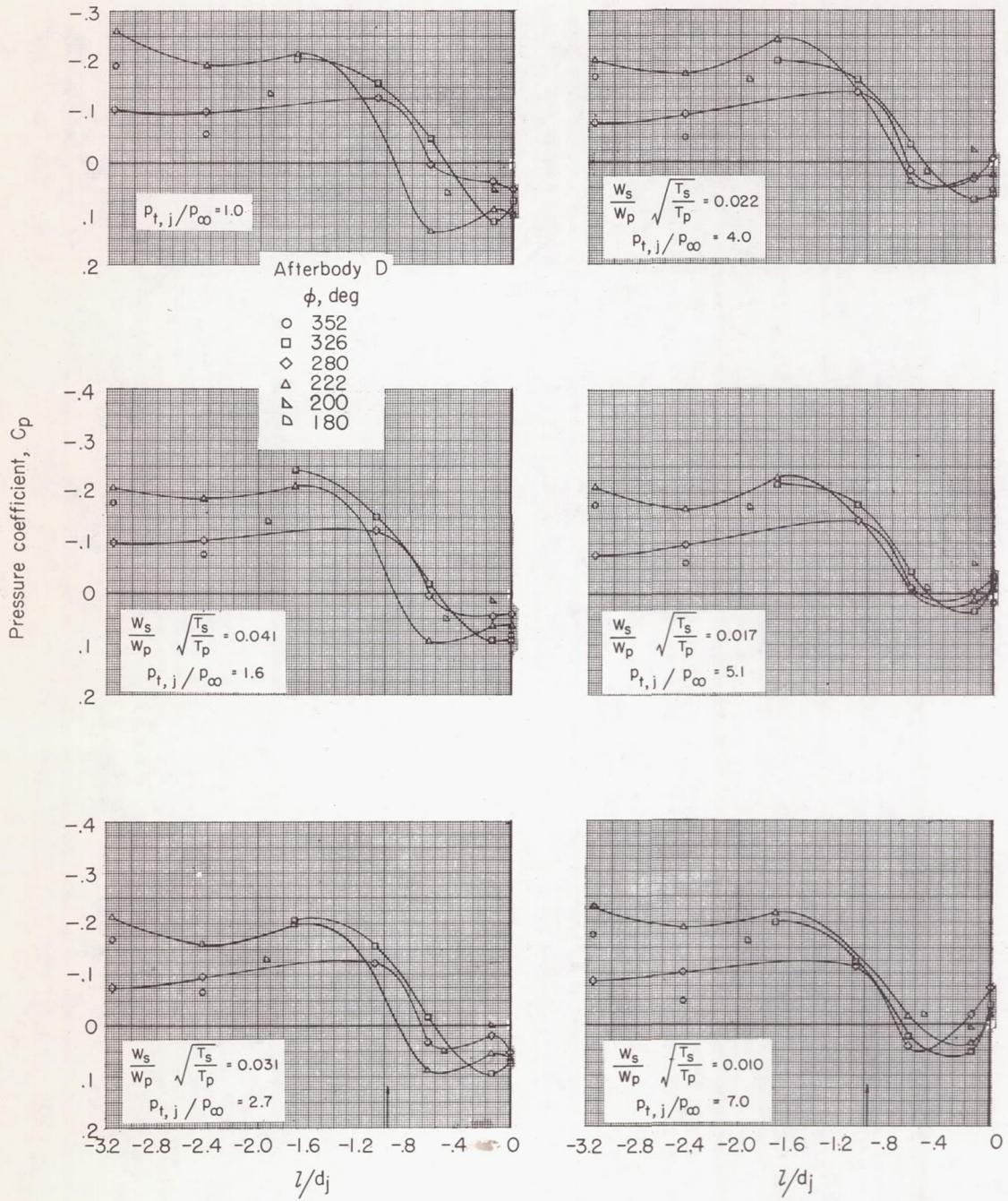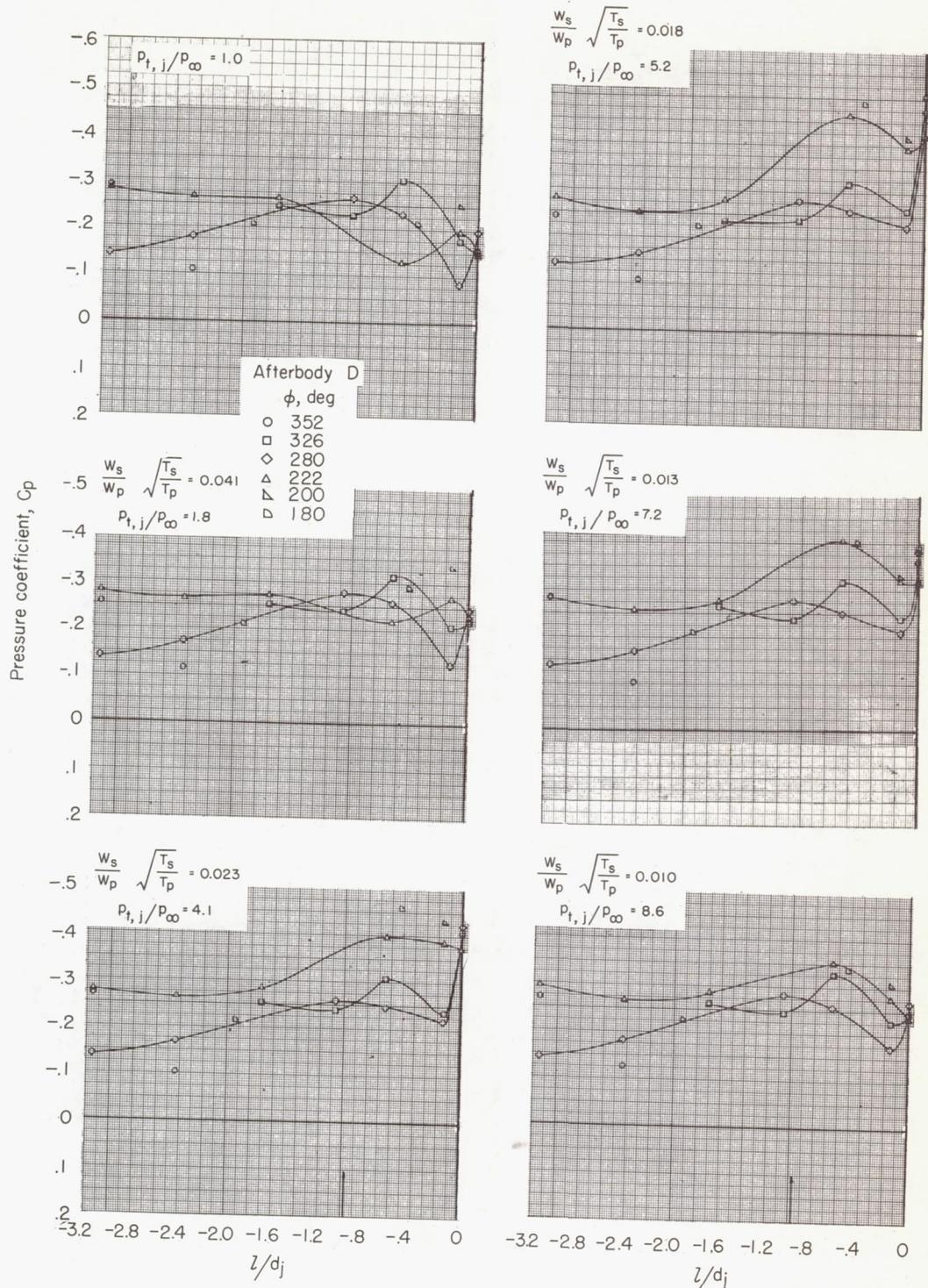
(d) M = 1.05; $\alpha = 0^\circ$.

Figure 9.- Continued.

(e) M = 1.10; α = 0°.

Figure 9.- Continued.

(f) M = 0.80; α = 3.5°.
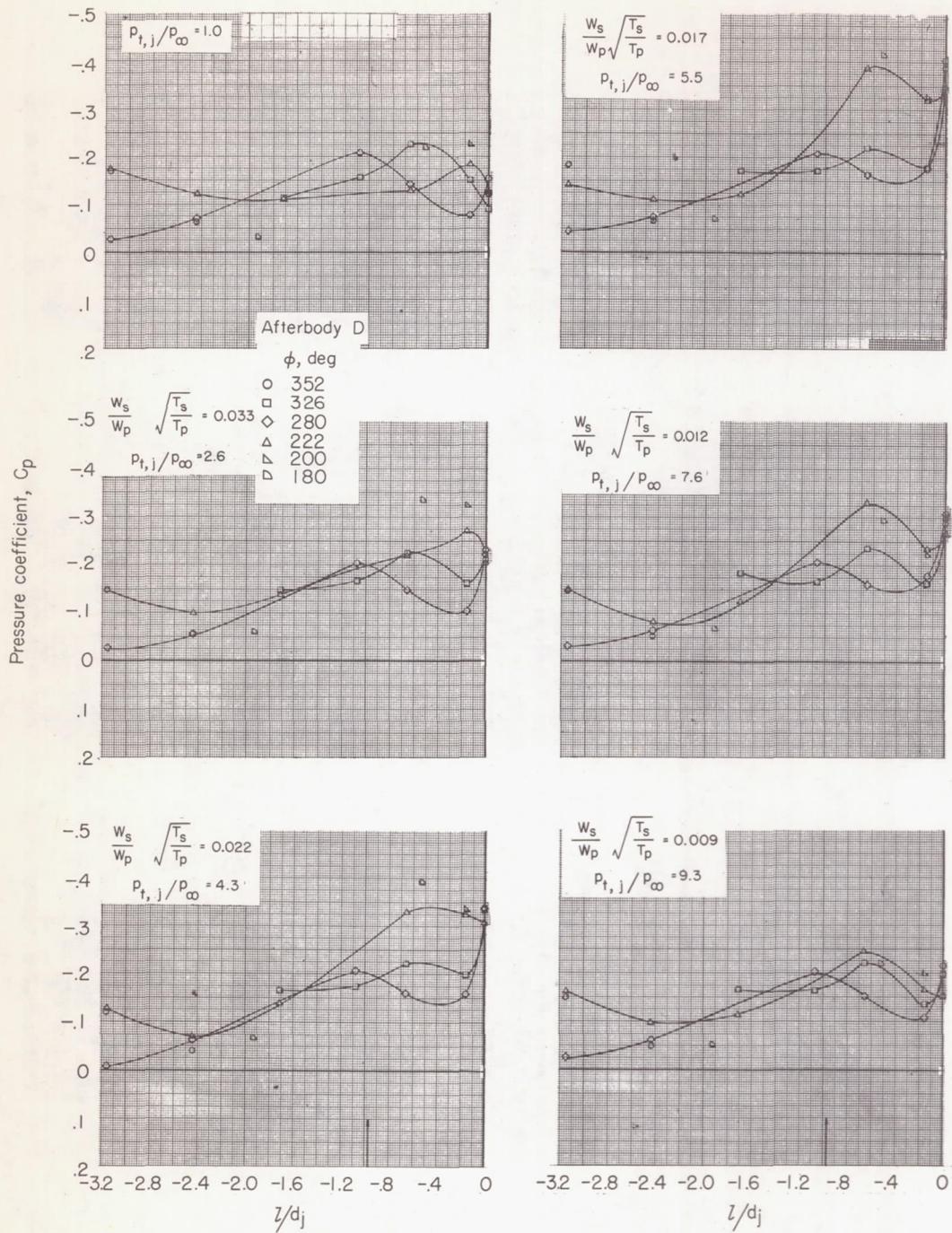
Figure 9.- Continued.

(g) M = 0.92; α = 3.5°.

Figure 9.- Continued.

(h) M = 1.00; α = 3.5°.
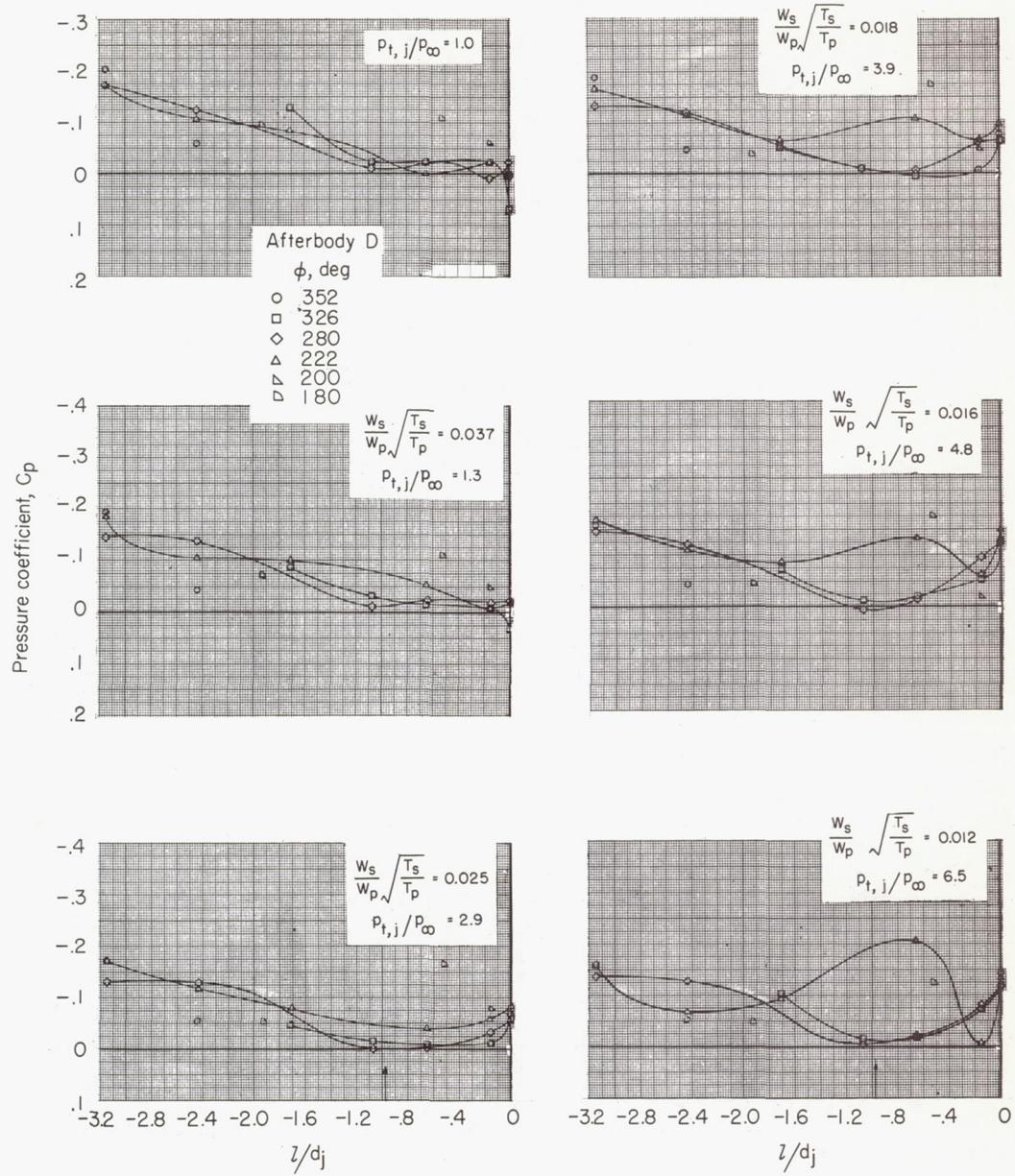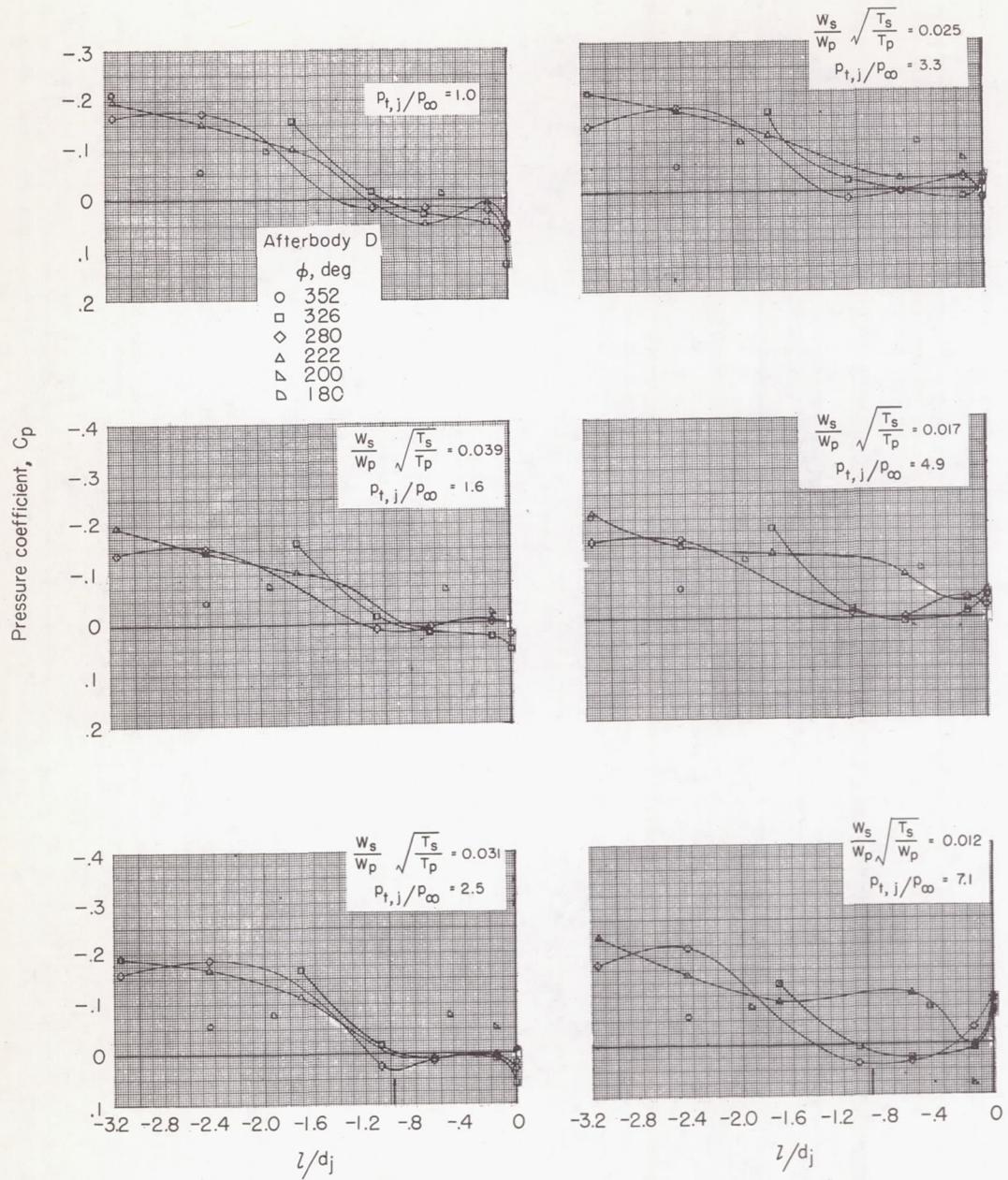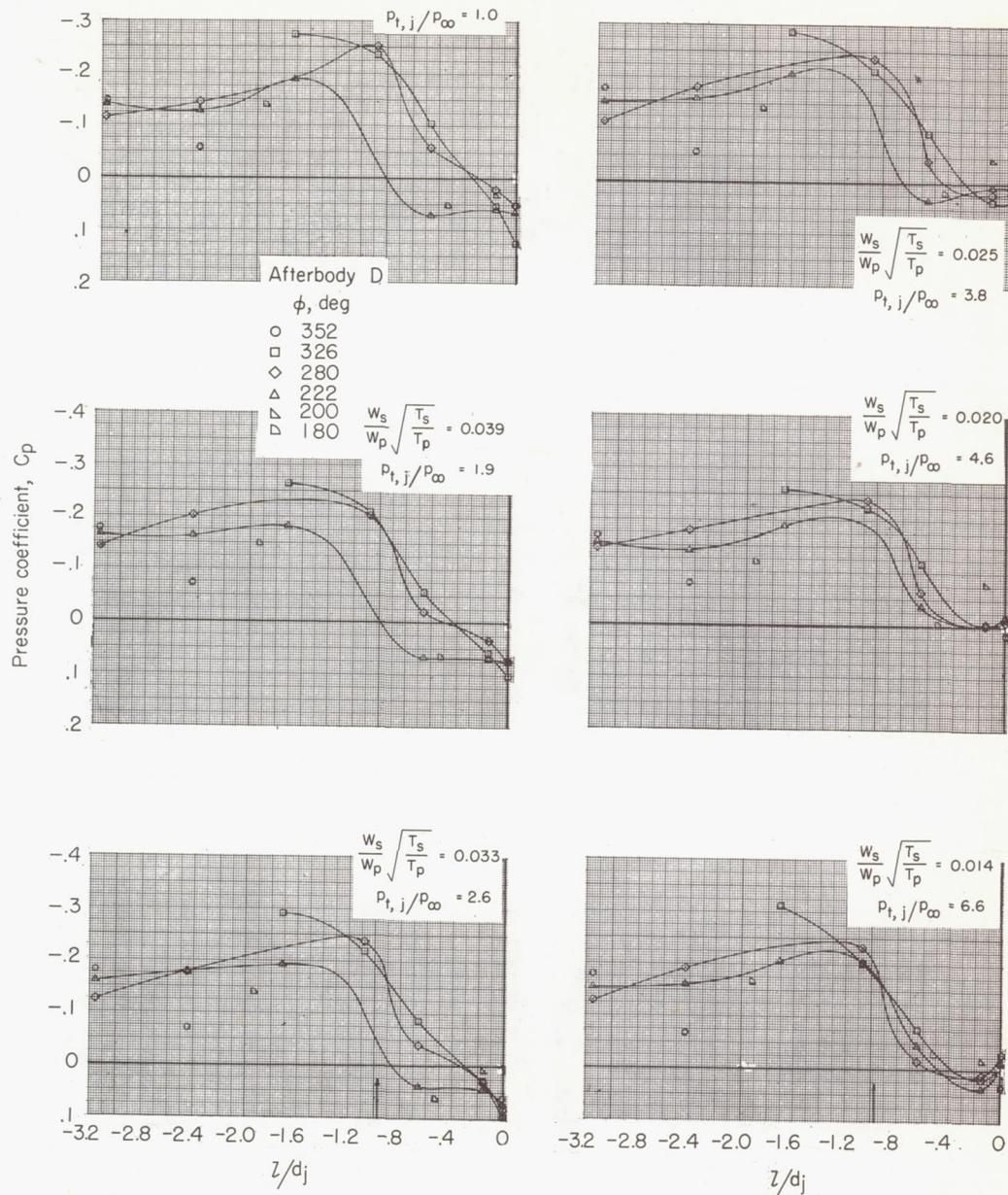
Figure 9.- Continued.
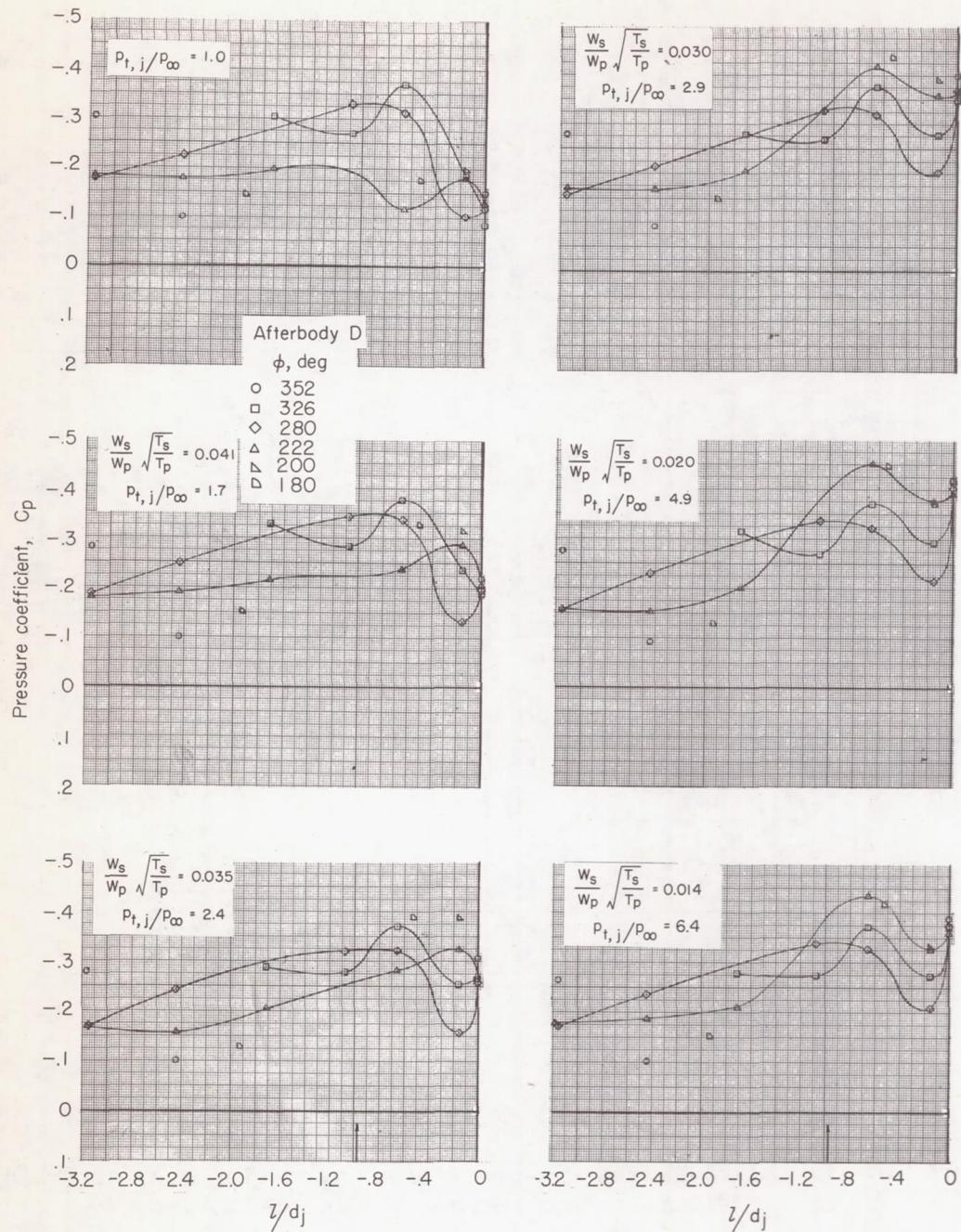
(i) M = 1.05; α = 3.5°.

Figure 9.- Concluded.
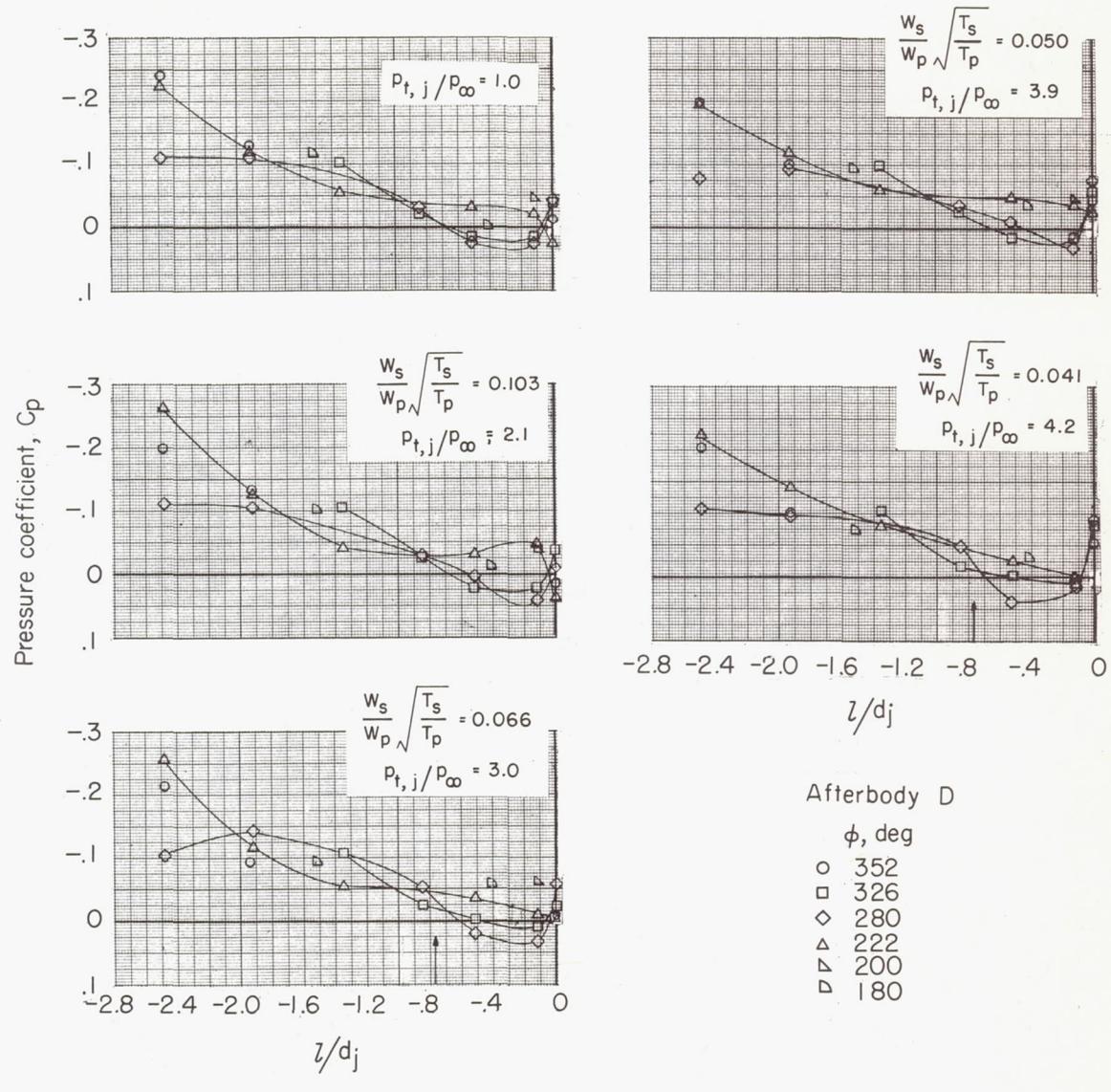
(a) M = 0.80.

Figure 10.- Examples of pressure-coefficient variation over afterbody D.
Afterburning nozzle; $\alpha = 0^O$; $i_t = -1.5^O$.
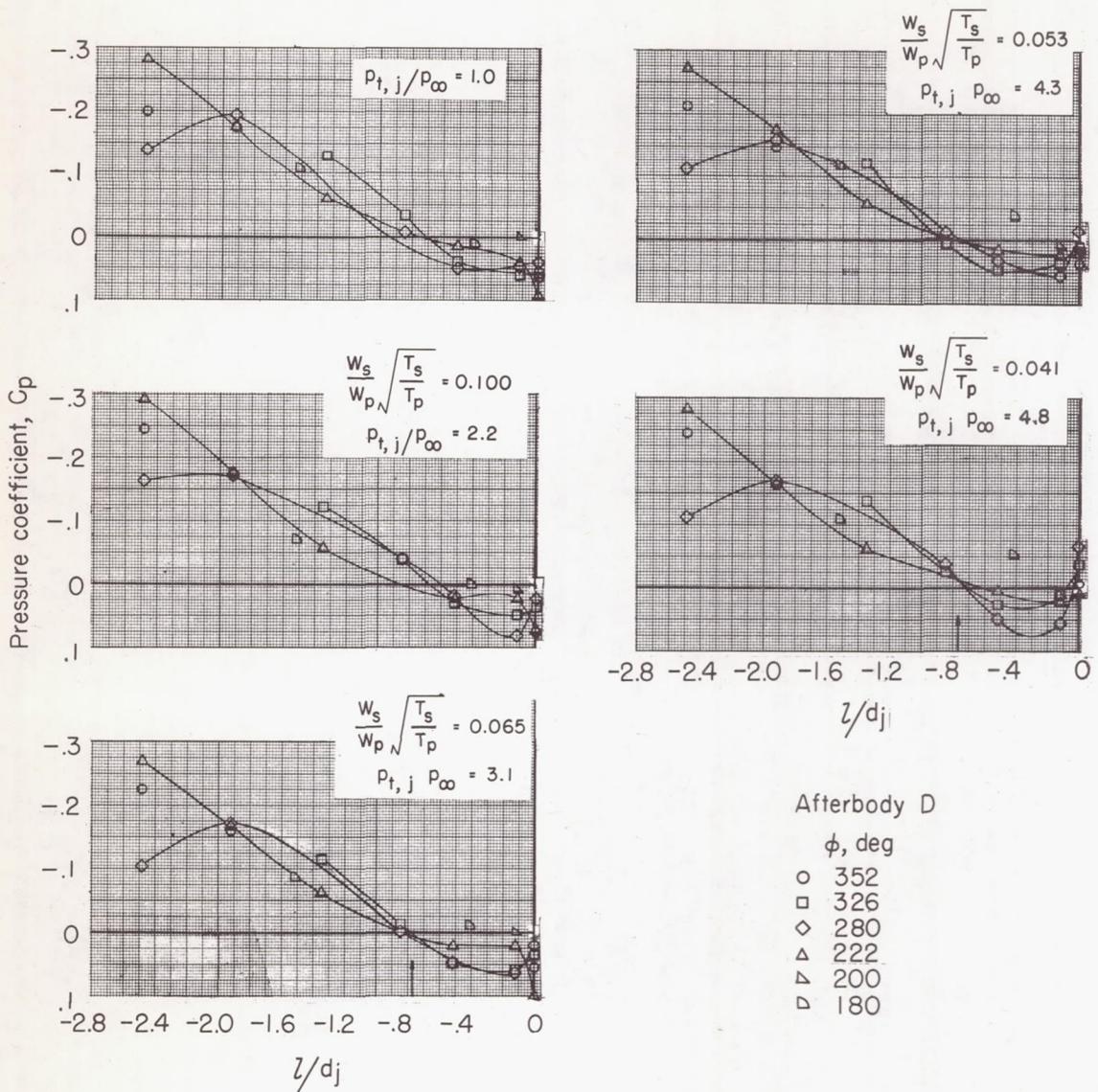
(b) M = 0.92.

Figure 10.- Continued.

(c) M = 1.05.
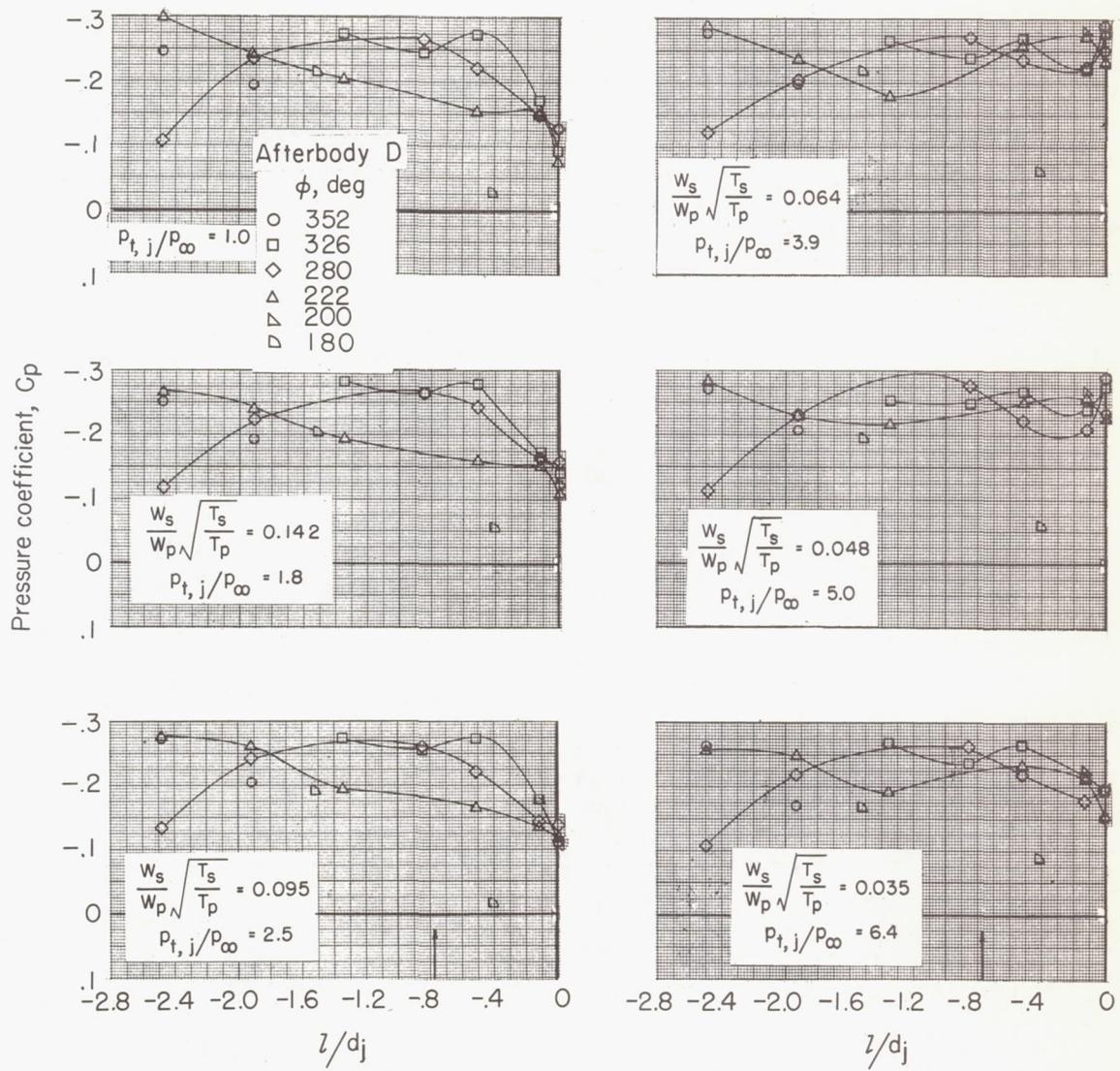
Figure 10.- Continued.
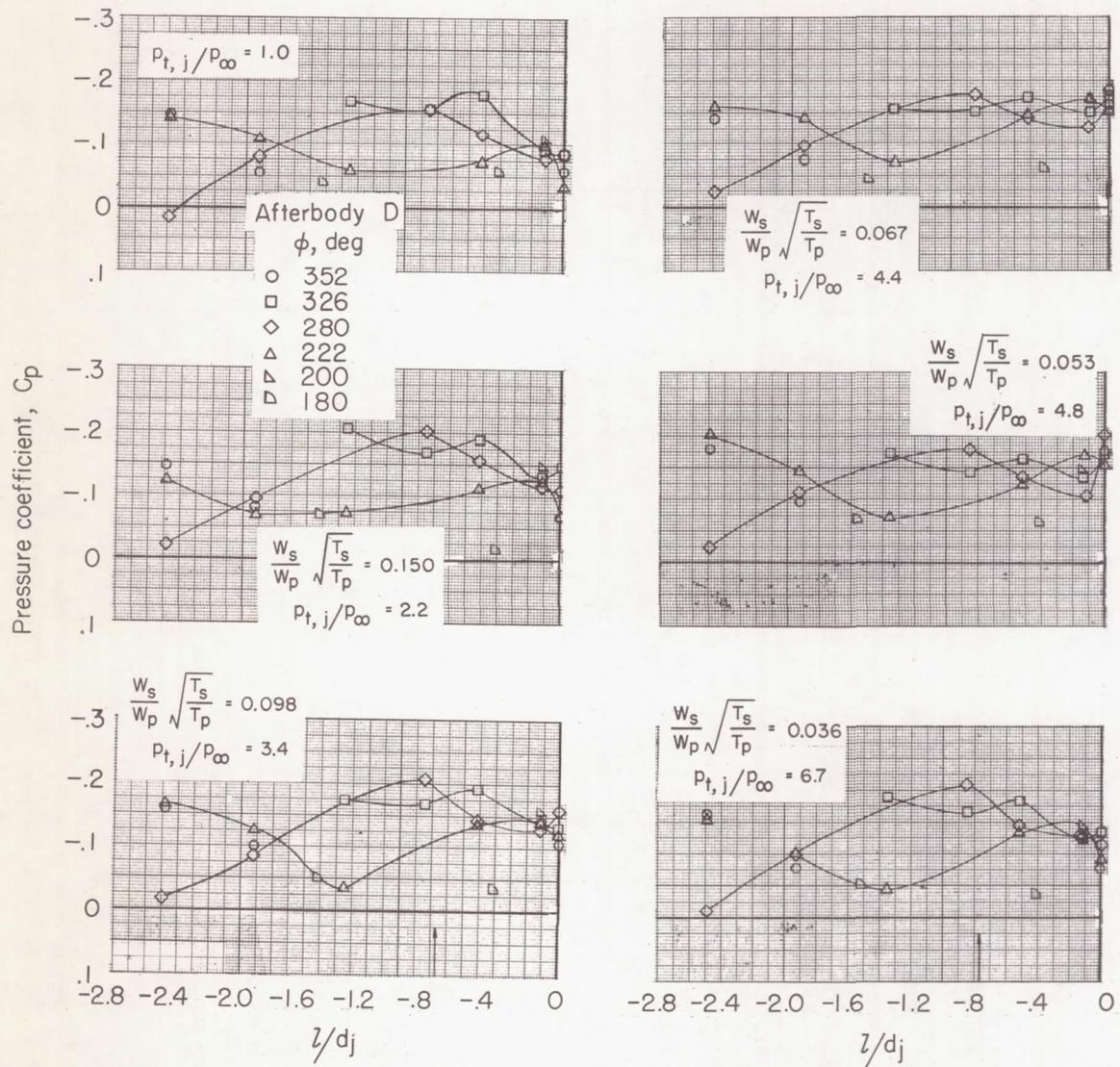
(d) M = 1.10.

Figure 10.- Concluded.
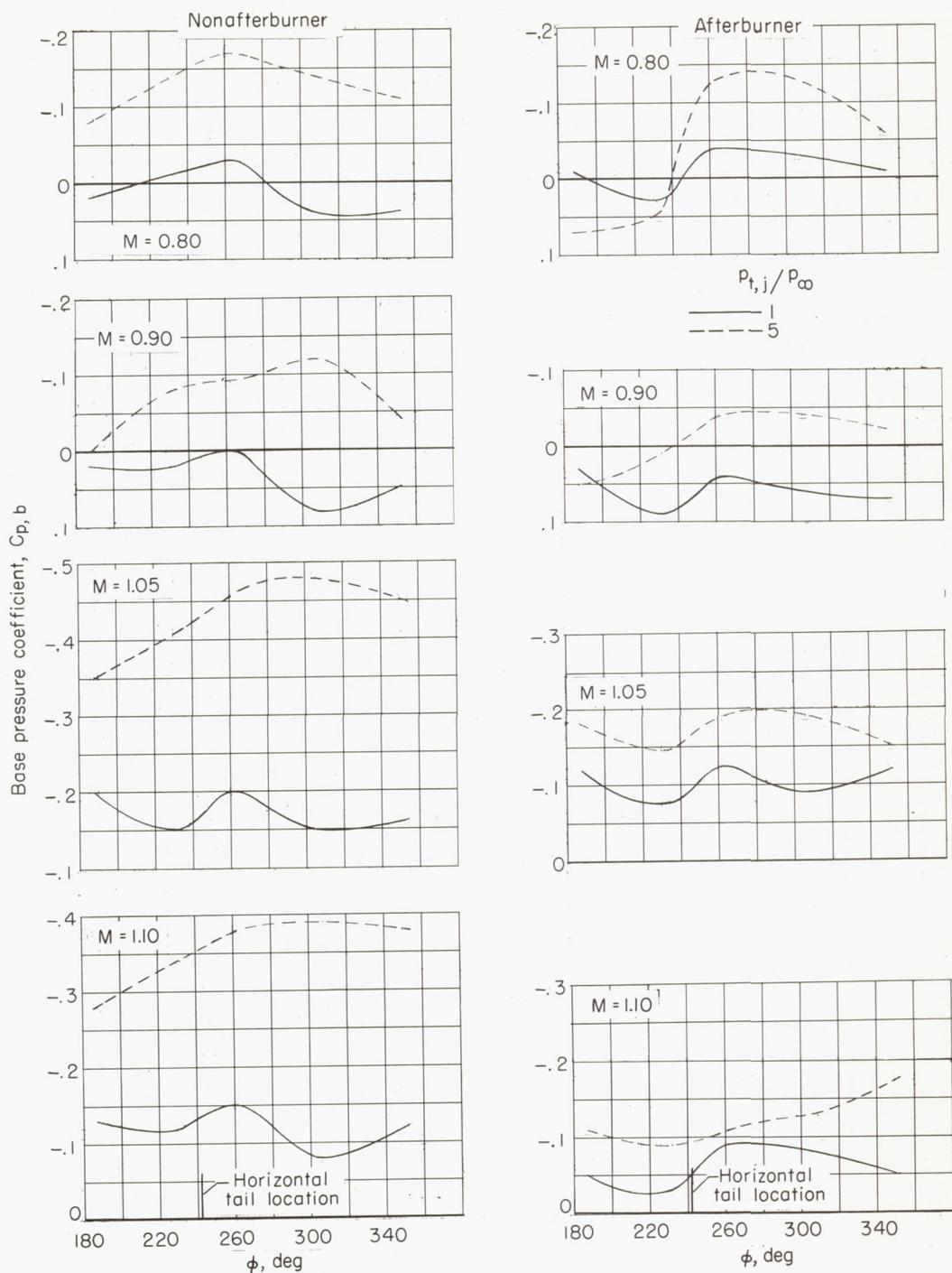
Figure 11.- Base pressure coefficient around the base annulus for several Mach numbers and primary jet total-pressure ratios. Afterbody D.
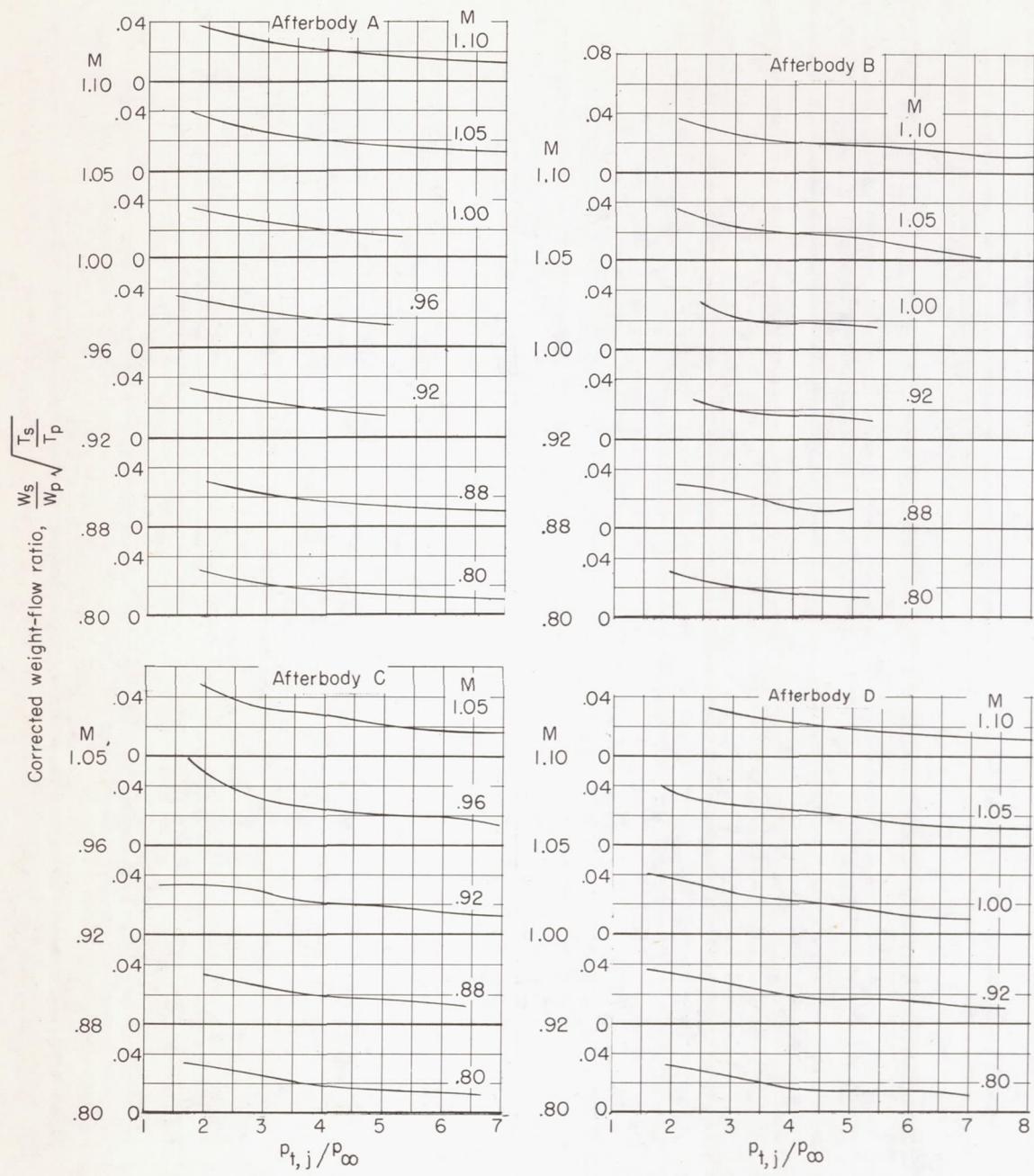
(a) Nonafterburner.

Figure 12.- Variation of corrected secondary weight-flow ratio with primary total-pressure ratio for all afterbodies.
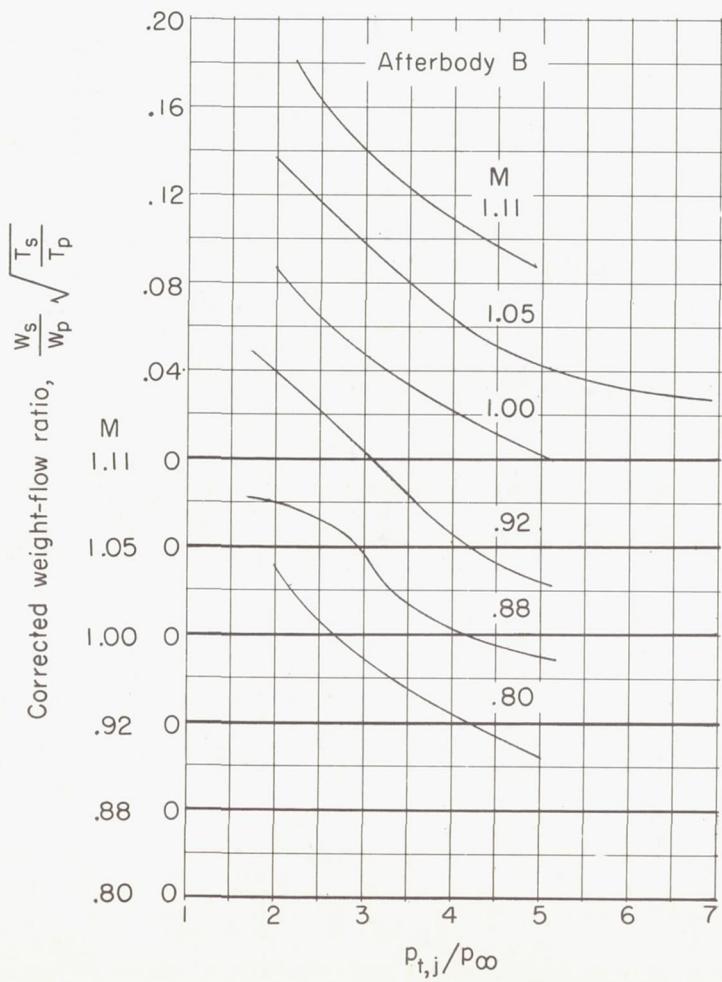
(b) Afterburner.

Figure 12.- Concluded.
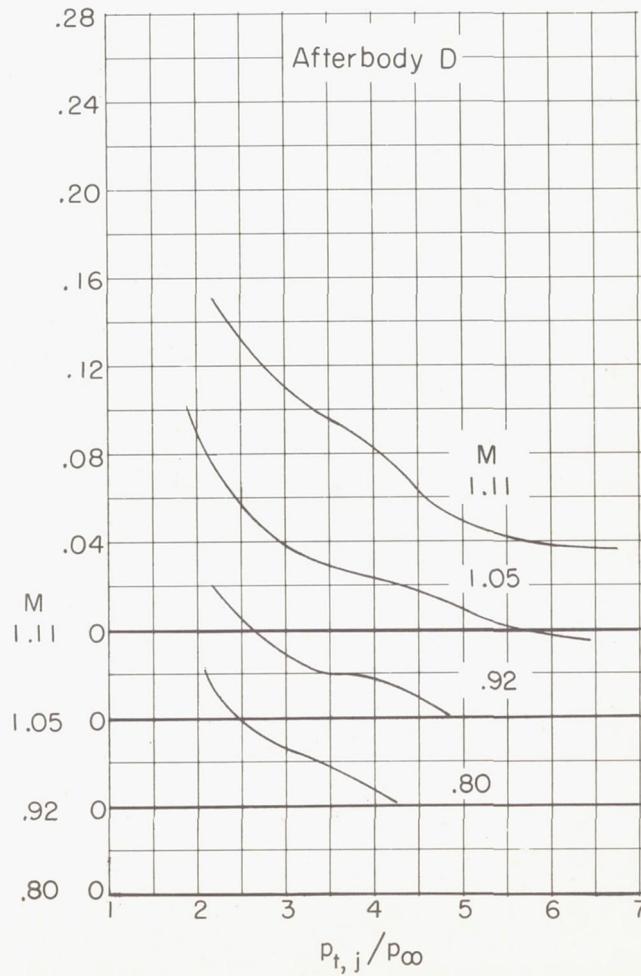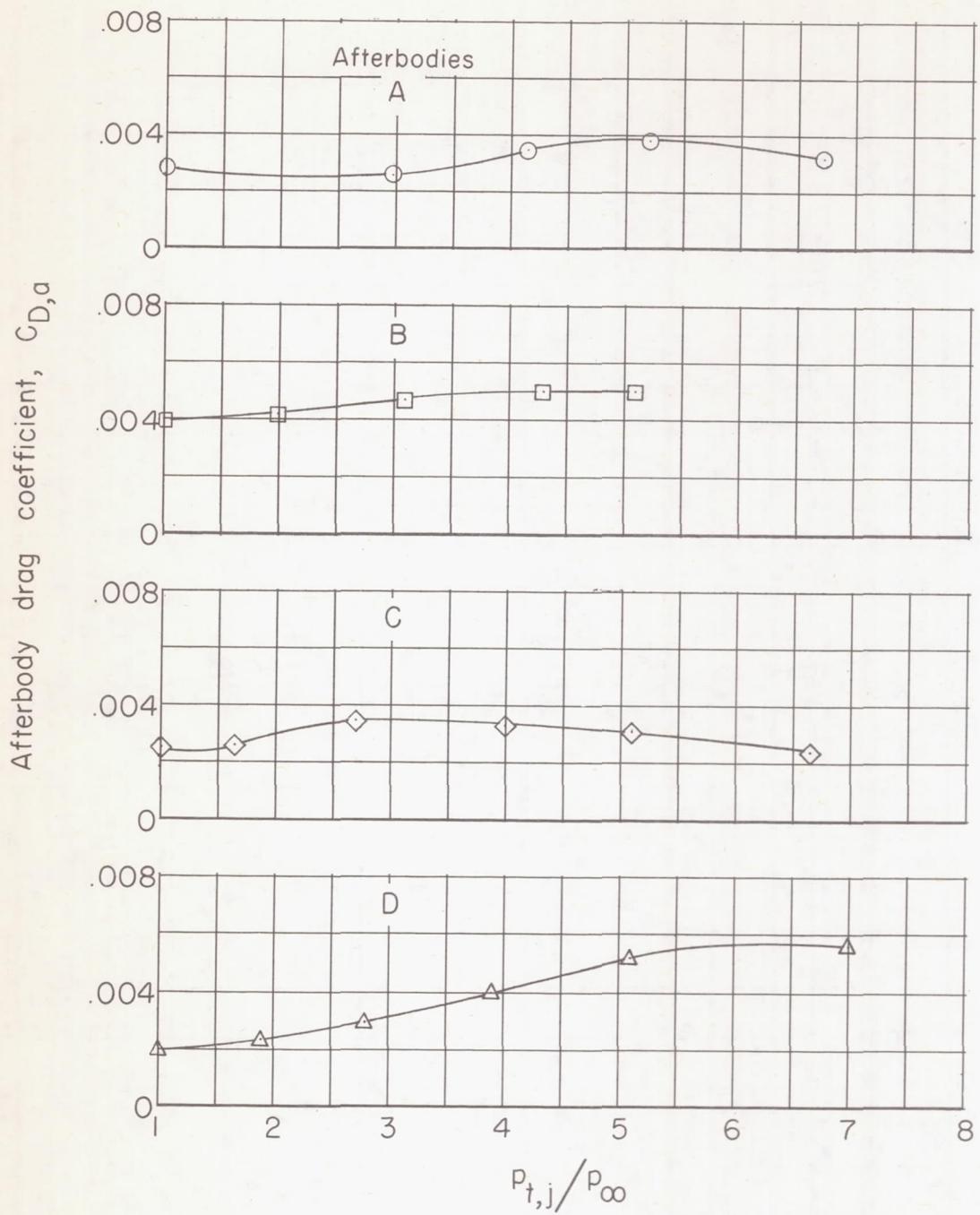
(a) M = 0.80.

Figure 13.- Effect of jet total-pressure ratio on afterbody drag
coefficient. Nonafterburning nozzle.
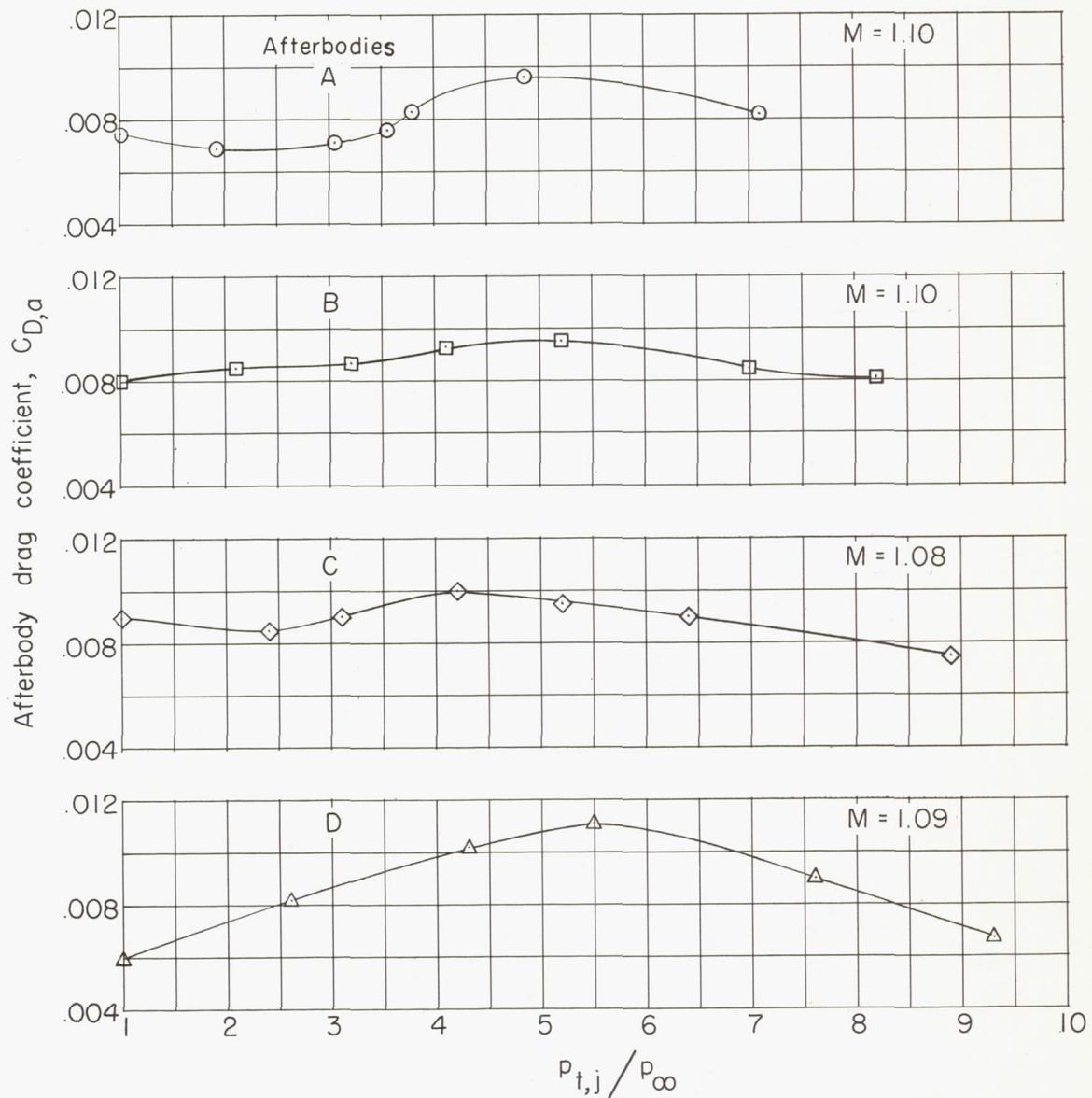
(b) M = 1.09 nominal.

Figure 13.- Concluded.
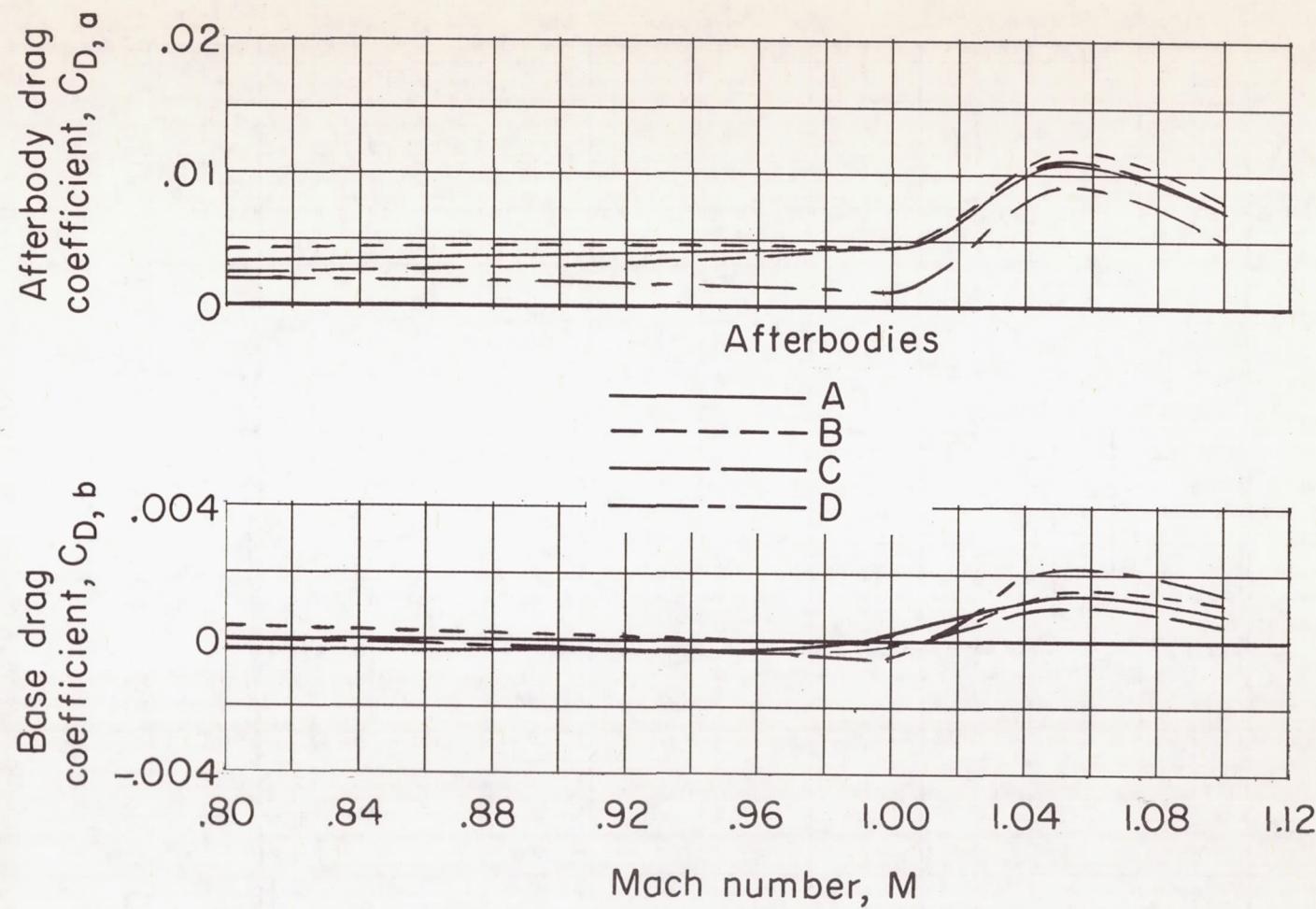
(a) Jet off.

Figure 14.- Variation of drag coefficient with Mach number for the afterbodies tested. Nonafterburning nozzle.

(b) Base drag coefficient $C_{D,b}$. Jet on.
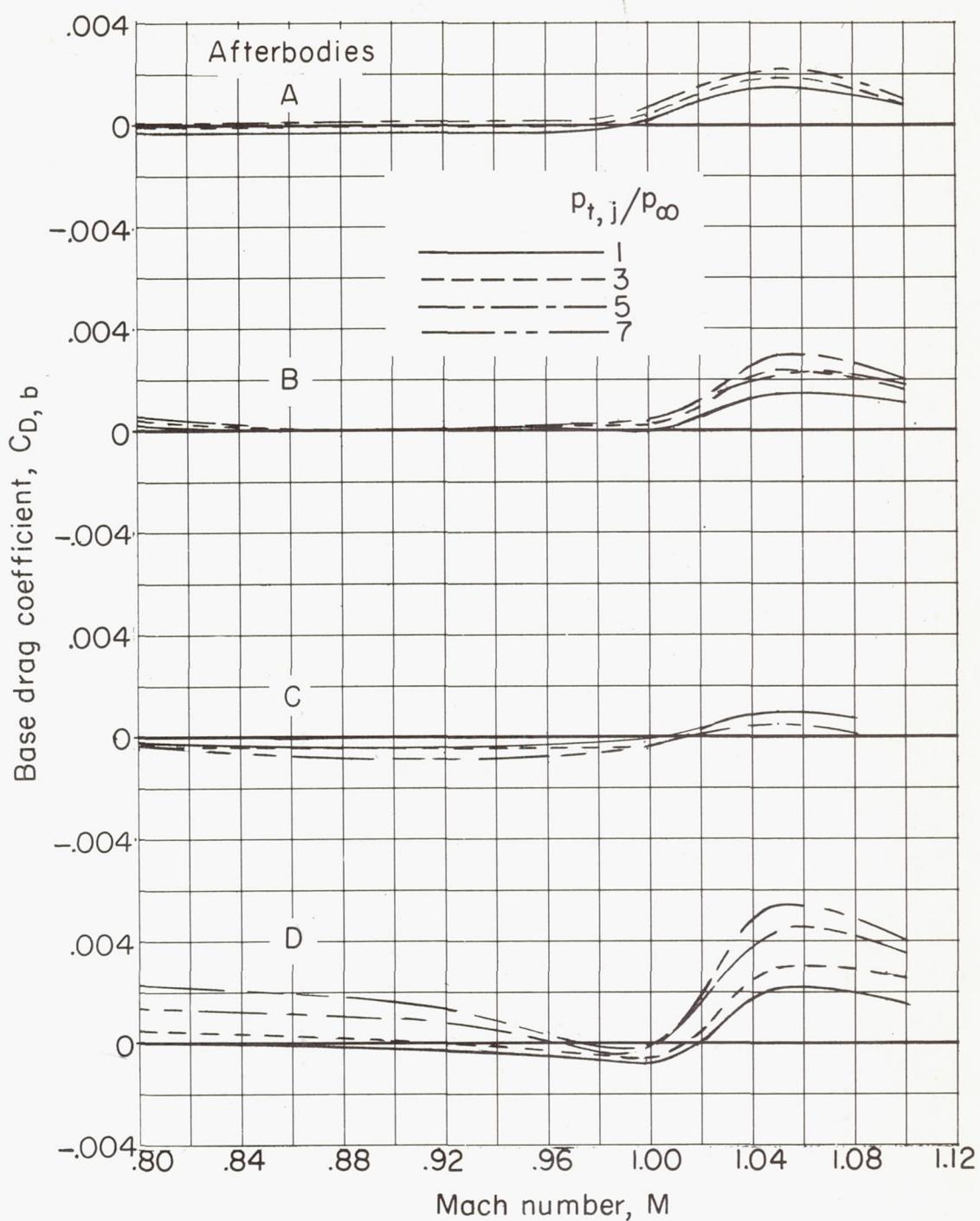
Figure 14.- Continued.
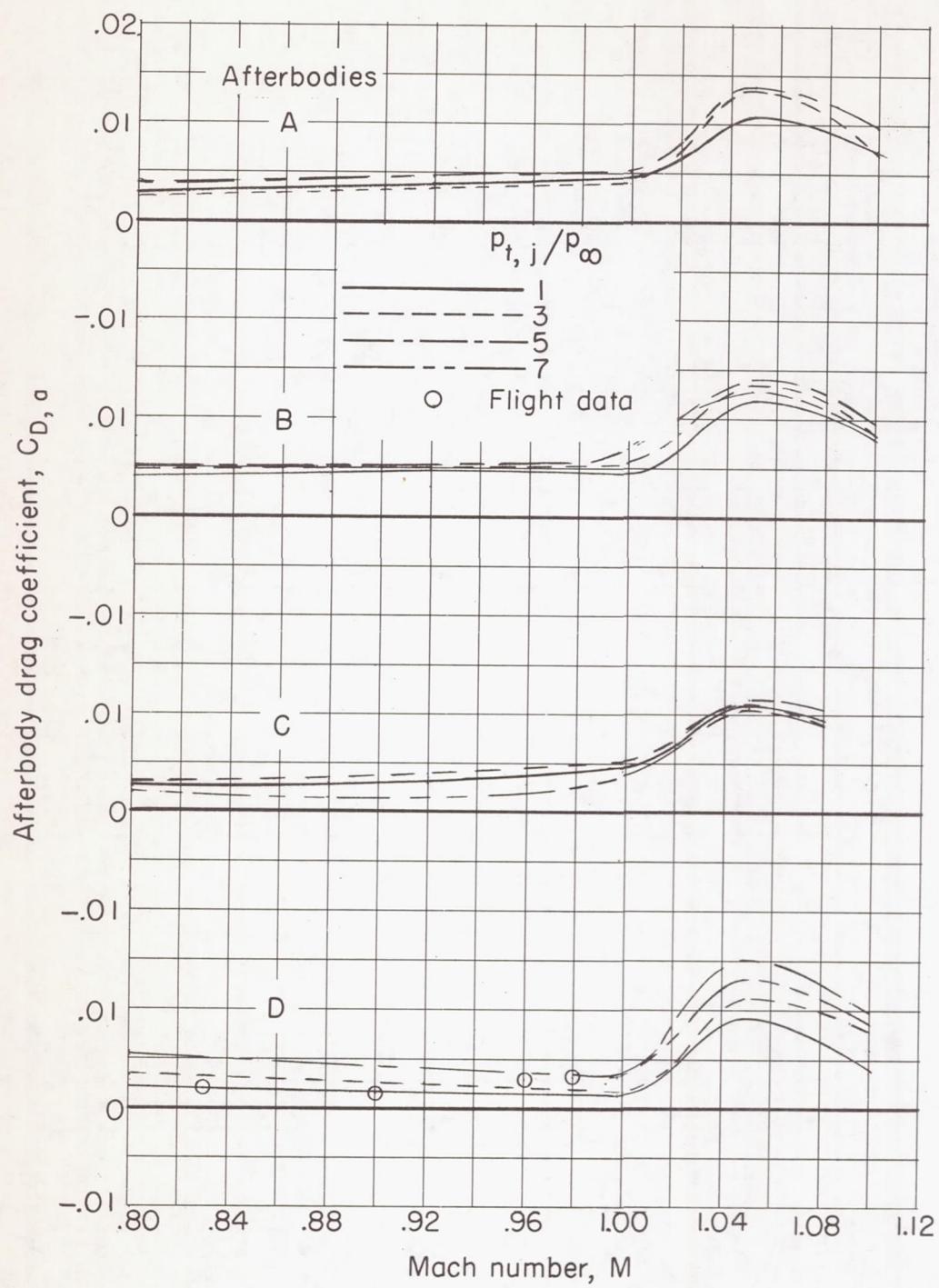
(c) Afterbody drag coefficient $C_{D,a}$. Jet on.

Figure 14.- Concluded.
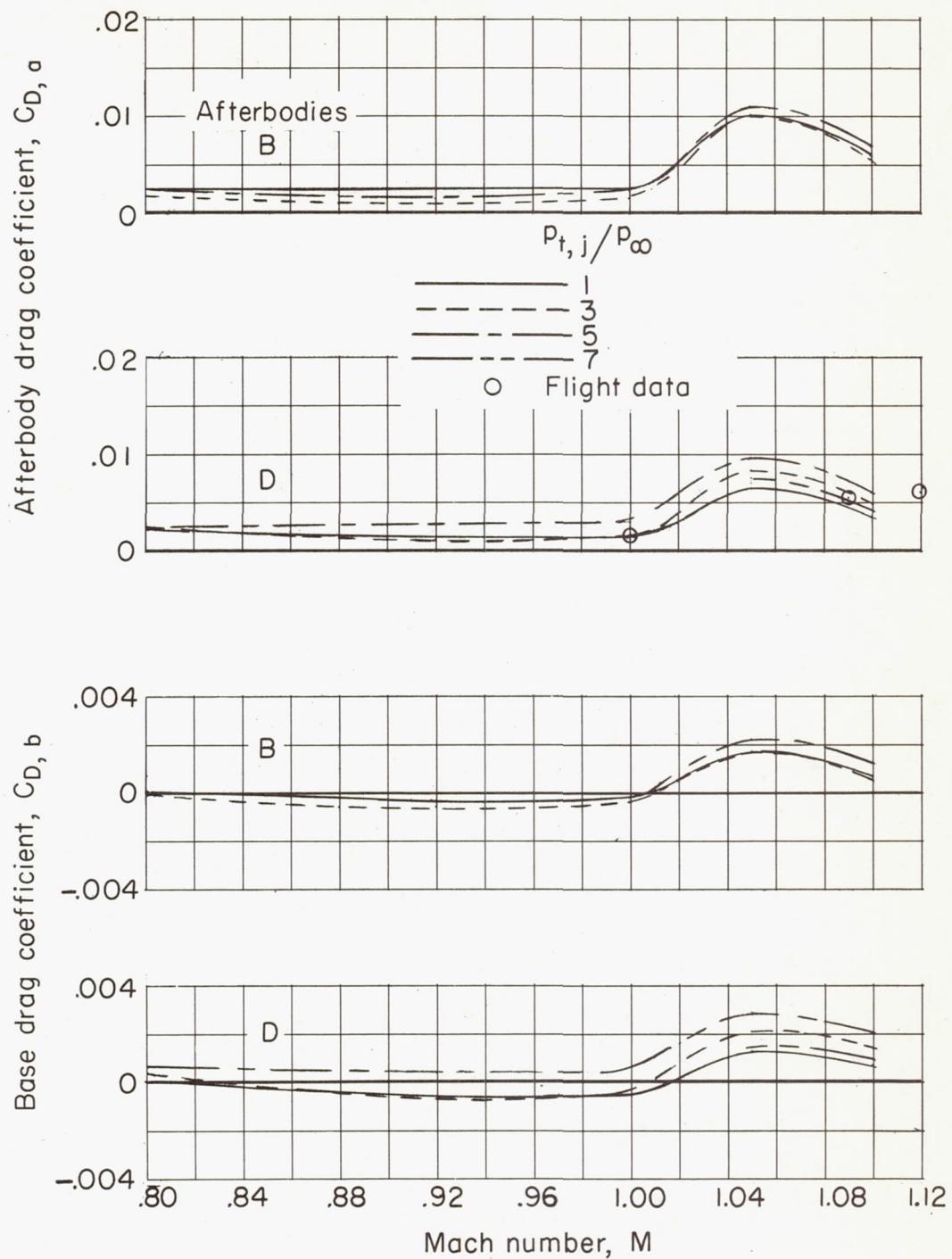
Figure 15.- Variation of drag coefficient with Mach number at several
values of primary jet total-pressure ratio.   Afterburning nozzle.
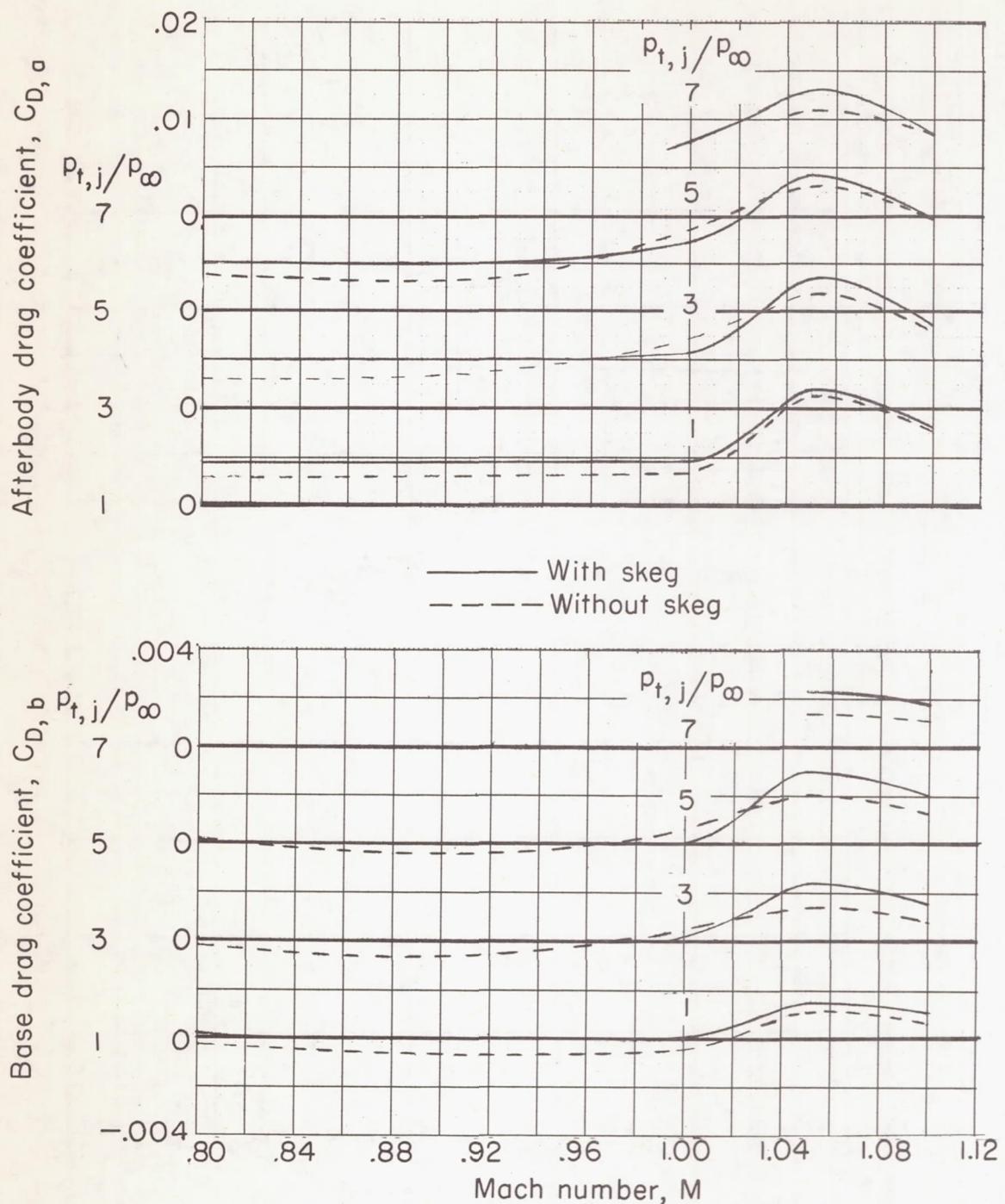
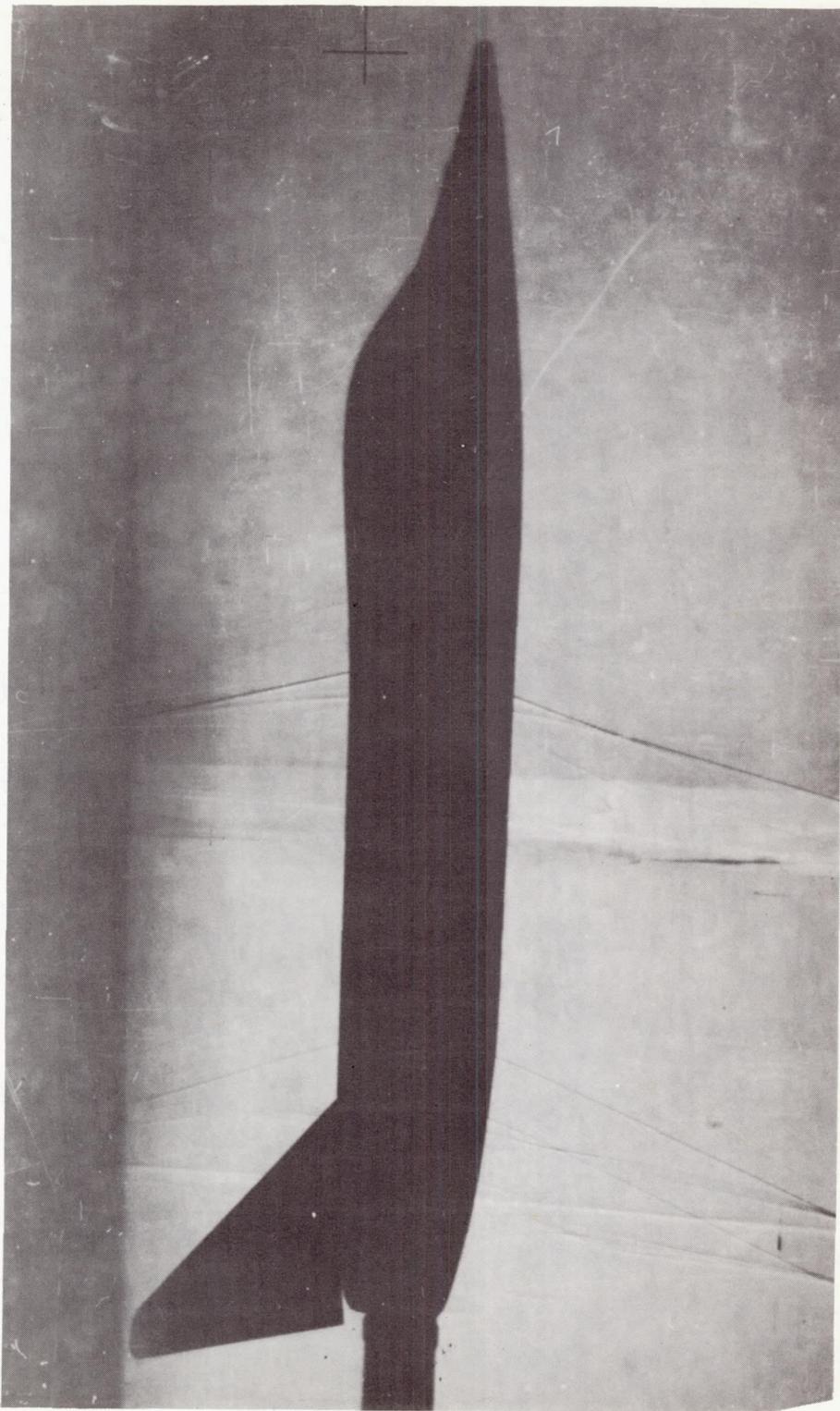Figure 16.- Effect of skeg on drag of afterbodies. Nonafterburning
nozzle.
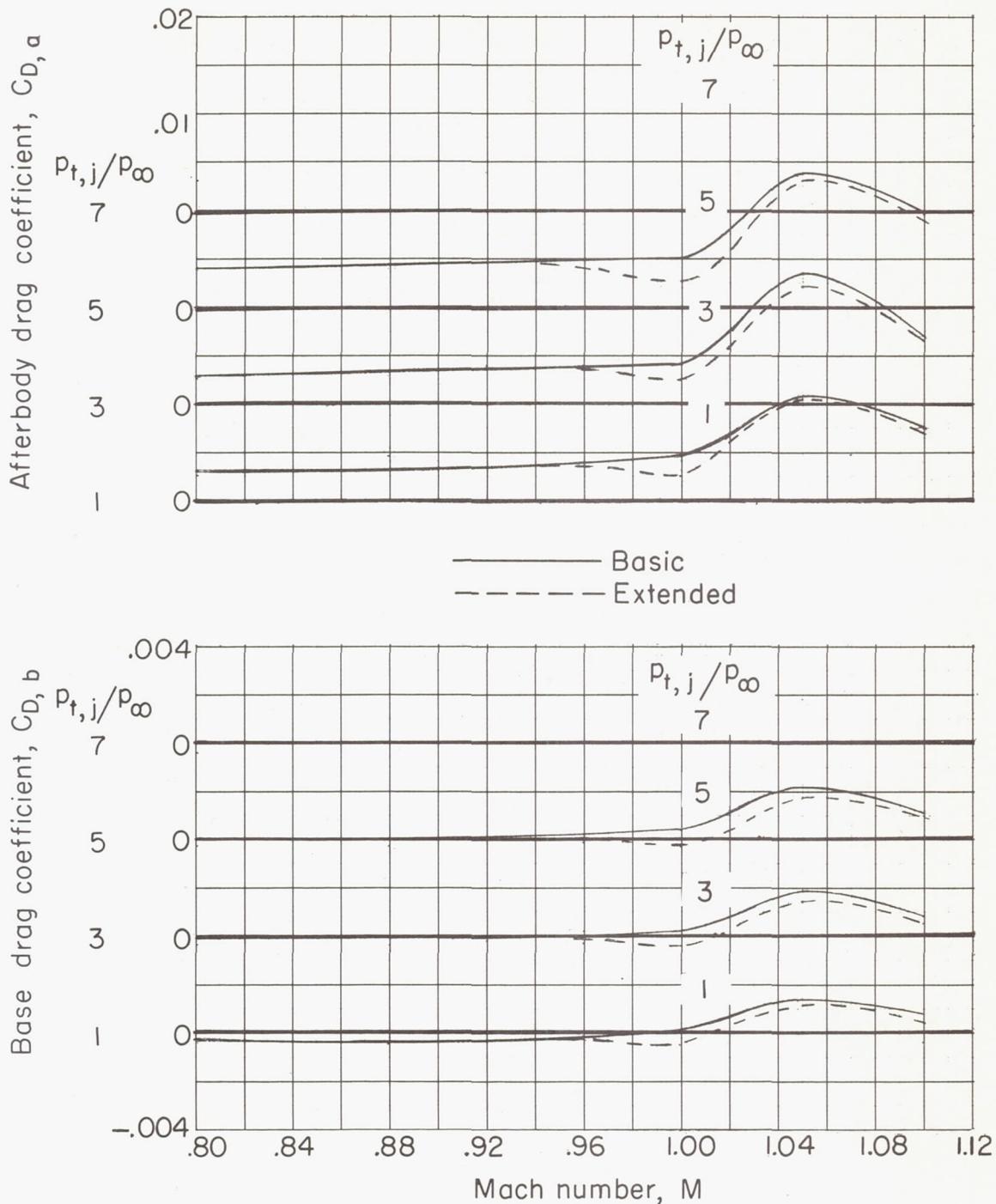
Figure 17.- Effect of extending wing-tip support fairings on drag coefficient on afterbody A.
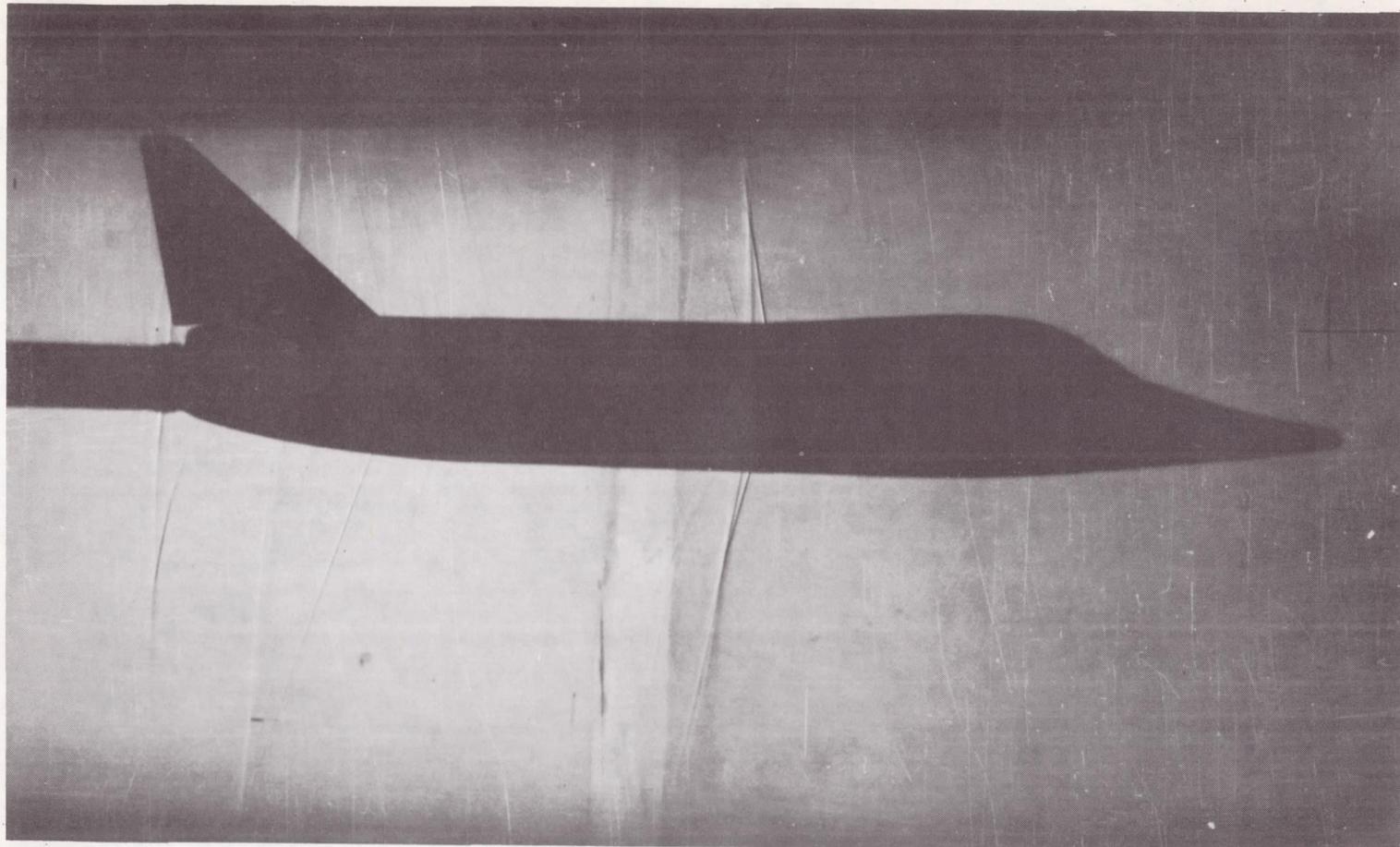
(a) Basic fairings.

L-57-2764

Figure 18.- Shadowgraphs illustrating complexity of flow field. M = 1.00; $p_{t,j}/p_\infty$ = 5.0.

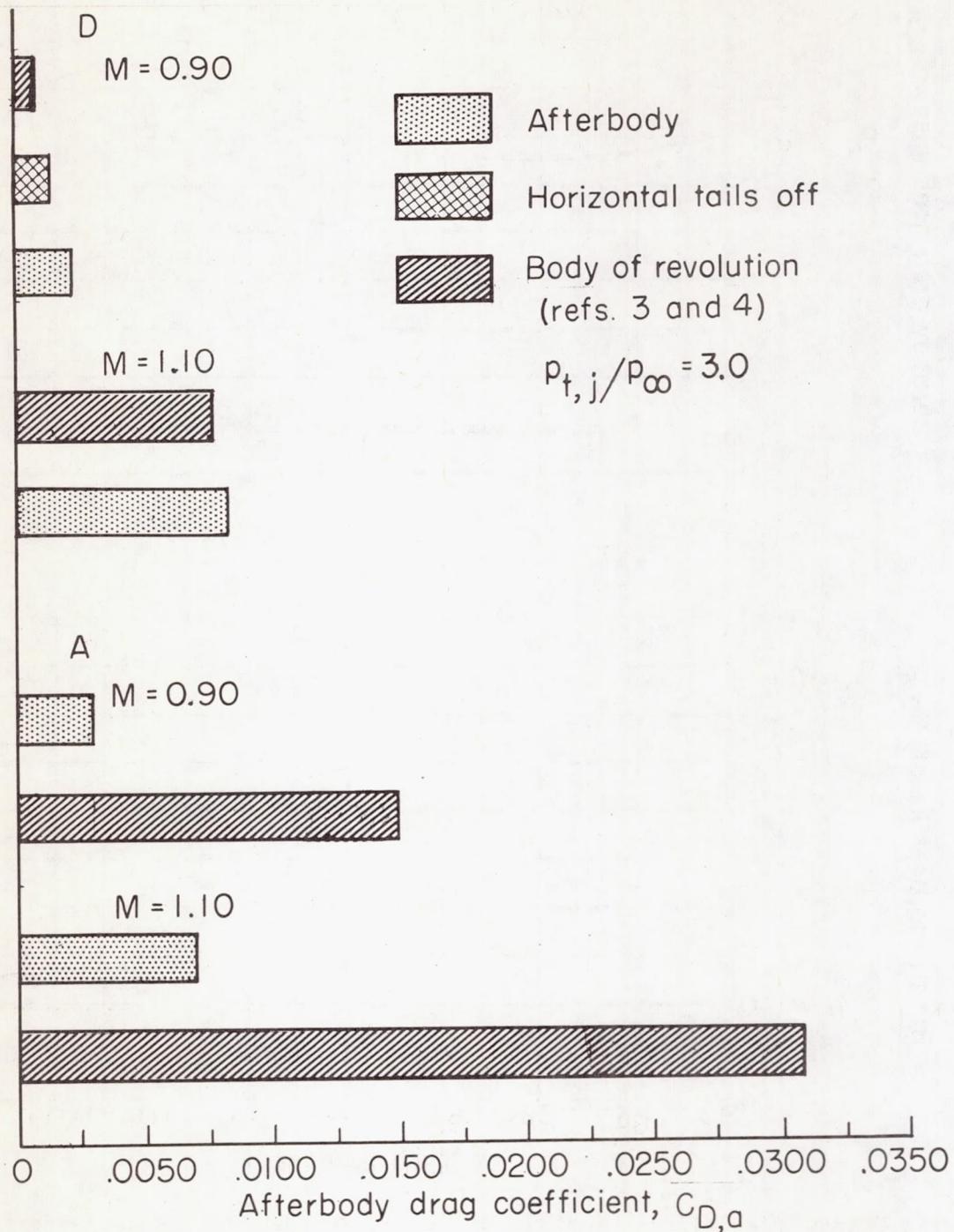(b) Extended fairings.   L-57-2765

Figure 18.- Concluded.

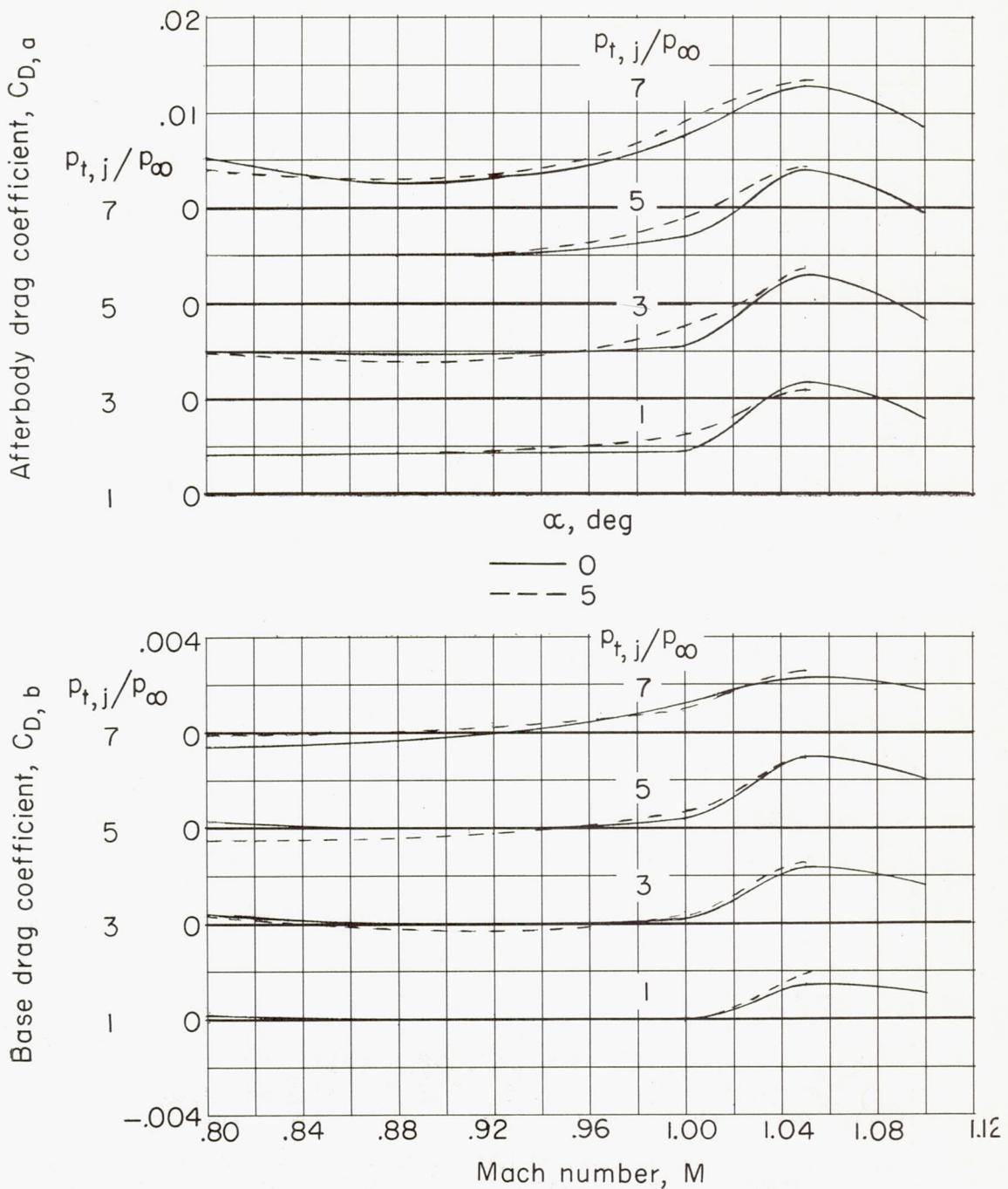Figure 19.- Effect of tail interference on afterbody drag coefficient.

Figure 20.- Effect of angle of attack on base and afterbody drag
coefficients of afterbody B.